Examining Terrain Effects on the Evolution of Precipitation and Vorticity of Typhoon Fanapi (2010) after Departing the Central Mountain Range of Taiwan

YAO-CHU WU,[a] MING-JEN YANG,[a] AND ROBERT F. ROGERS[b]

[a] *National Taiwan University, Taipei, Taiwan*
[b] *Hurricane Research Division, NOAA/AOML, Miami, Florida*

(Manuscript received 3 August 2021, in final form 17 March 2022)

ABSTRACT: Typhoon Fanapi (2010) made landfall in Hualien in Taiwan at 0100 UTC 19 September 2010 and left Taiwan at 1200 UTC 19 September 2010, producing heavy rainfall and floods. Fanapi's eyewall was disrupted by the Central Mountain Range (CMR) and reorganized after leaving the CMR. High-resolution simulations (nested down to 1-km horizontal grid size) using the Advanced Research Weather Research and Forecasting (WRF) Model, one simulation using the full terrain (CTL) and another set of simulations where the terrain of Taiwan was removed, were analyzed. Precipitation areas were classified into different subregions by a convective–stratiform separation algorithm to assess the impact of precipitation structure on Fanapi's eyewall evolution. The percentage of deep convection increased from 9% to 20% when Fanapi underwent an eyewall reorganization process while departing the CMR. In the absence of terrain, moderate convection occupied most of the convective regions during the period when Fanapi moved across Taiwan Island. The low-level total vorticity stretching within the convective, stratiform, and weak-echo regions in the no-terrain experiment were of similar magnitudes, but the total vorticity stretching within the convective region at low levels was dominant in the CTL experiment. Total vorticity stretching in the region of deep convection increased after eyewall reorganization, and later became stronger than that in the moderate convection region. In the absence of the CMR, total vorticity stretching in moderate convection dominated. The total vorticity stretching within the deep convective region in the CTL experiment played an essential role in the reorganization of Fanapi's eyewall through a bottom-up process.

SIGNIFICANCE STATEMENT: When a tropical cyclone makes landfall on Taiwan Island, the Central Mountain Range (CMR) usually disrupts the eyewall and changes the percentage of convective and stratiform precipitation areas. Unlike most typhoons whose eyewalls are weakened after landfall, Typhoon Fanapi's eyewall reorganized and the percentage of deep convection increased from 9% to 20% when Fanapi moved to the west side of the CMR. Understanding how the terrain of Taiwan weakened the vortex circulation of Typhoon Fanapi during landfall and rebuilt the vorticity and eyewall after landfall is important to improve the forecast of TCs with similar track and intensity in the future.

KEYWORDS: Hurricanes/typhoons; Precipitation; Nonhydrostatic models

1. Introduction

In the tropics, convective precipitation is frequently associated with strong vertical velocities (usually greater than the terminal velocities of hydrometeors) and intense rainfall rates. In contrast, stratiform precipitation is defined as a less active precipitation area with widespread and weak vertical motion (Houze 1997). For a typical tropical cyclone (TC), there are many convective cells embedded in the primary rainbands that spiral into the eyewall. The overturning flow within the TC secondary circulation transports frozen hydrometeors (ice crystals or snowflakes) up to upper levels. Then the ice particles descend to form stratiform precipitation around the convective region (Atlas et al. 1963; Hence and Houze 2012).

Convective–stratiform separation algorithms can be used to distinguish convective from stratiform precipitation based on the differences between rainfall rates, radar reflectivity, and vertical velocity. Poujol et al. (2020) classifies the algorithms based on structural and temporal characteristics. The former uses strong positive spatial anomalies to identify the convective updrafts (e.g., Churchill and Houze 1984), while the latter uses rainfall rate intensity threshold to separate the convective and stratiform regions (e.g., Tremblay 2005). Although rainfall rates may not be highly related to microphysical processes, temporal algorithms are commonly used for rain gauge data in poor-spatial-resolution cases. The texture algorithms that require high-spatial-resolution data like radar data or cloud-resolving model outputs are more reasonable.

The separation between convective and stratiform precipitation is helpful to analyze the kinematic and microphysical structures of convective cells embedded in stratiform clouds and precipitation. In an observational study, Didlake and Houze (2013a) used a convective–stratiform separation algorithm on airborne Doppler radar measurements in Hurricane Rita (2005) to compare the composite of three-dimensional velocities in convective cells at different radii within the

Denotes content that is immediately available upon publication as open access.

Corresponding author: Ming-Jen Yang, mingjen@as.ntu.edu.tw

DOI: 10.1175/MWR-D-21-0205.1

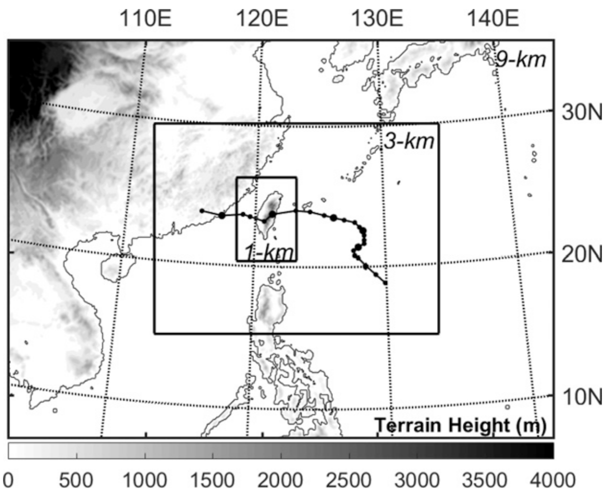

FIG. 1. Three nested domains (with the horizontal grid sizes of 9, 3, and 1 km) of the WRF Model used in this study. The 6-hourly best track of Fanapi from the JTWC, starting from 1200 UTC 14 Sep and ending at 0600 UTC 20 Sep 2010 (large dots denote the position at 0000 UTC), is indicated. Terrain height on the 9-km grid is shaded. From Yang et al. (2018).

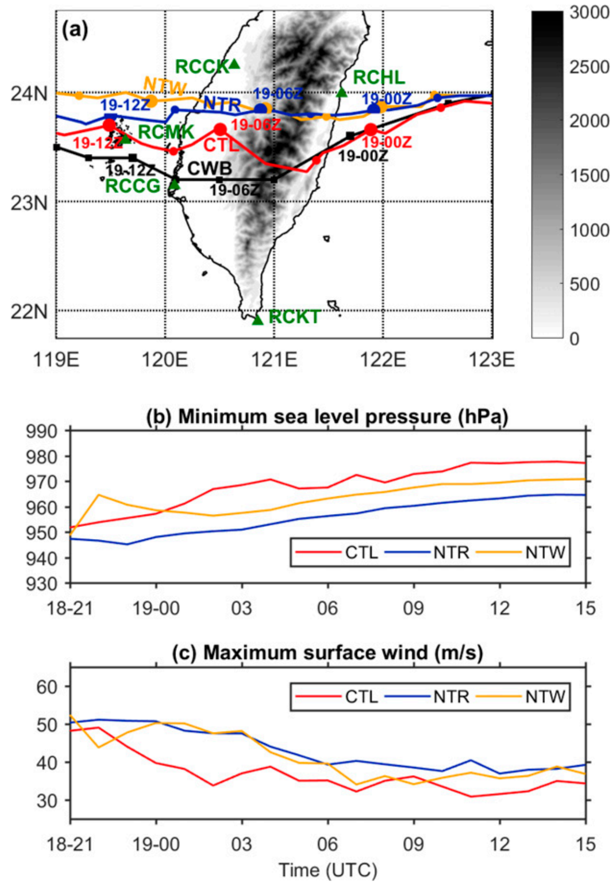

FIG. 2. (a) TC Fanapi's tracks from the CWB best track analysis (black), the CTL (red), NTR (blue), and NTW (orange) experiments. Big dots along the track indicate the 6-hourly TC center positions, and small dots along the track indicate the 3-hourly TC center positions. The green triangles indicate the locations of ground-based radars (RCHL, RCCK, RCMK, RCCG, and RCKT). The shaded area indicates the terrain height of CMR. Time series of (b) minimum sea level pressure and (c) maximum surface wind in for CTL (red), NTR (blue), and NTW (orange) experiments.

inner-core rainbands. They found that supergradient flows that led to convergence and convective cell development were essential for secondary eyewall formation. Rogers et al. (2020) implemented a convective–stratiform separation algorithm in airborne Doppler radar measurements of Hurricane Hermine (2016). They found that low-level vorticity was amplified through vorticity stretching and tilting processes in deep convection, while the thermodynamic environment was modified into one more favorable for moderate convection. The large portion of moderate convection maintained the mesoscale circulation structure with a broad area of enhanced stretching and tilting to overcome the moderate vertical wind shear at the early stage. In a modeling study, Rogers (2010) applied a convective–stratiform separation algorithm on high-resolution MM5 model output to examine the interaction between convection and the vortex and the evolution of vertical mass flux during the rapid intensification of Hurricane Dennis (2005).

The studies mentioned above show the multitude of ways that precipitation structure and evolution can impact TC structure. Another example where precipitation may affect TC structure is through the disruption and subsequent reorganization of a TC eyewall upon encountering terrain. Typhoon Fanapi (2010) made landfall in Hualien (over the east coast of Taiwan) at 0100 UTC 19 September and left Taiwan at 1200 UTC 19 September 2010, producing heavy rainfall and floods. Fanapi's eyewall was broken down by the Central Mountain Range (CMR) of Taiwan while the TC vortex circulation was over Taiwan Island. When Fanapi moved to the western side of the CMR, its eyewall reorganized and heavy rainfall accumulated in southwestern Taiwan. This reformation process is in contrast to most typhoons, whose eyewalls remain disorganized and weaken after landfall.

Eyewall reorganization processes of Typhoon Fanapi (2010) were documented by both radar observations and high-resolution model simulations. Liou et al. (2016) used an advanced technique called the Wind Synthesis System using Doppler Measurements (WISSDOM) to retrieve the three-dimensional wind field during the period of eyewall reconstruction. Typhoon Fanapi (2010) is a unique typhoon case in which dual-Doppler radar observations from two Doppler radars (one ground-based operational radar and one mobile research radar) were available to document the kinematic and

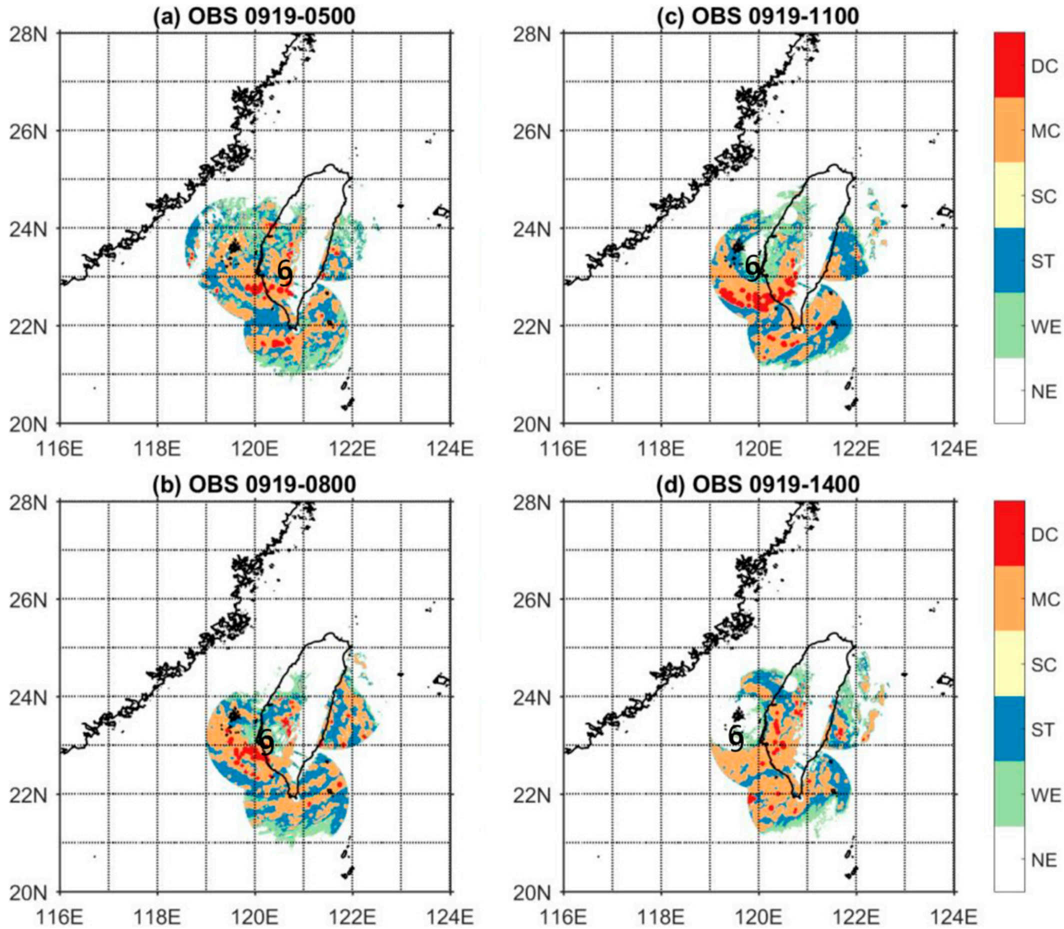

FIG. 3. The plan view of radar-observed precipitation-regime classification at 2-km height using the convective–stratiform separation algorithm. The TC symbol indicates the location of the typhoon center.

precipitation structure within Fanapi's inner core, and vertical hot towers (VHTs) over land were documented for the first time in the literature. Yang et al. (2018) conducted a high-resolution WRF Model simulation (with finest horizontal grid size of 1 km) to compare the VHTs over the open ocean and over land. The VHTs over land had weaker maximum updrafts (7–8 m s^{-1}), narrower diameters (7–11.5 km), and shallower depths (6.5–9 km) than those over the ocean. The VHTs moved toward the CMR along the spiral rainbands and transported vorticity-rich air from lower levels to middle levels. Therefore, Fanapi underwent a bottom-up eyewall reorganization process, which is uncommon in the literature for landfalling typhoons. Most studies on VHTs were performed using airborne or spaceborne instruments for oceanic TCs, but Liou et al. (2016) and Yang et al. (2018) are some of the relatively few studies to examine the role of VHTs in TC eyewall reformation under the influence of terrain from observational and modeling perspectives.

In this study, two main scientific issues are addressed to examine the impacts of the CMR on landfalling Typhoon Fanapi: 1) Does the presence of the CMR play a key role in the eyewall regeneration for Fanapi? 2) How is eyewall regeneration related to the change of precipitation regime and vorticity forcing for Fanapi? The methodology of this study is presented in sections 2 and 3 discusses the precipitation regions of Typhoon Fanapi. A vorticity budget to determine the dominant vorticity generation processes and the associated precipitation types to understand the reformation process is given in section 4. Concluding remarks are in section 5.

2. Methodology

A control (CTL) simulation with the full complex CMR topography and two sensitivity experiments with no Taiwan terrain were conducted by using the Advanced Research Weather Research and Forecasting (WRF) Model (ARW-WRF v3.3.1;

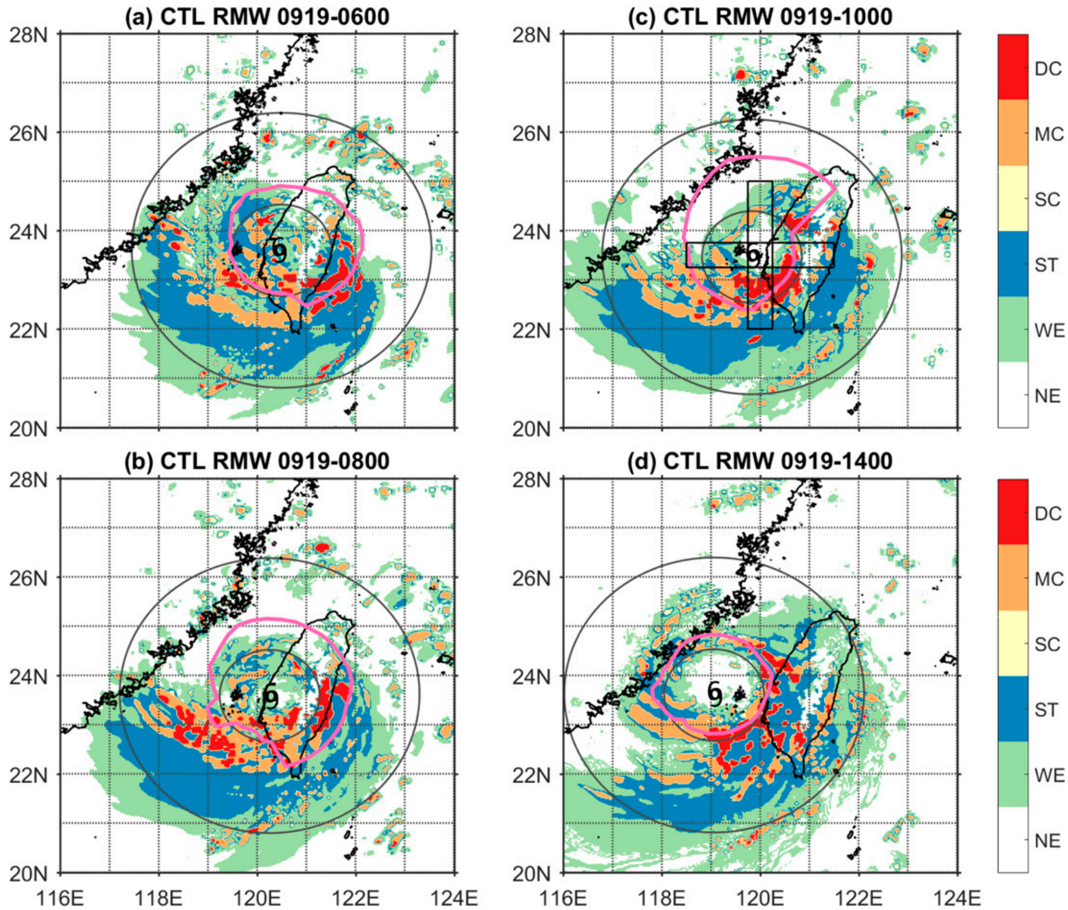

FIG. 4. As in Fig. 3, but for the CTL experiment. The inner circle indicates the radius of 100 km from the TC center, and the outer one indicates the radius of 300 km from the TC center. Radius of maximum wind (RMW) is indicated by the thick pink contour. Two boxes in (c) indicate the horizontal positions of two vertical cross sections shown in Fig. 16.

Skamarock et al. 2008). The CTL simulation, which ran from 0000 UTC 18 September to 0000 UTC 20 September 2010, captured the breakdown and reorganization of the eyewall of Typhoon Fanapi. The horizontal grid sizes of the triply nested grid were 9, 3, and 1 km. A total of 55 eta levels are implemented in the vertical direction. The European Centre for Medium-Range Weather Forecasts/Tropical Ocean Global Atmosphere (ECMWF/TOGA) analysis datasets with 1.125° horizontal grid spacing were used as the initial and boundary conditions. The boundary conditions were updated every 6 h. Figure 1 shows the three nested-grid domains. Physical parameterization schemes used in the model include the Grell–Dévényi ensemble cumulus parameterization (Grell and Dévényi 2002), the double-moment Morrison microphysics parameterization (Morrison et al. 2005; Morrison and Gettelman 2008), Rapid Radiative Transfer Model (RRTM) longwave radiation parameterization (Mlawer et al. 1997), Dudhia (1989) shortwave parameterization, and the Yonsei University (YSU) planetary boundary layer parameterization (Hong and Pan 1996). Note that the cumulus scheme is used in the 9-km grid only, because the grid sizes of the 3- and 1-km grids are fine enough to explicitly resolve convection. Details of the simulation verification were presented in Yang et al. (2018).

To determine whether the stronger vortex circulation in the no-Taiwan-terrain (NTR) run (compared with the CTL run) plays an important role in the upward transport of positive vorticity by stronger convection (to be discussed in section 4), a no-terrain-weak experiment (NTW) with a warmer, drier, and weaker TC inner core is created from the CTL run. Inside the inner core (with radius of less than 100 km) for this NTW experiment, temperature is increased by 2 K below 850 hPa, moisture is reduced by 10% below 700 hPa, and wind speed is reduced by 30% below 200 hPa. Hydrostatic balance is imposed vertically, and gradient-wind balance is imposed horizontally to require the balance between wind and mass fields.

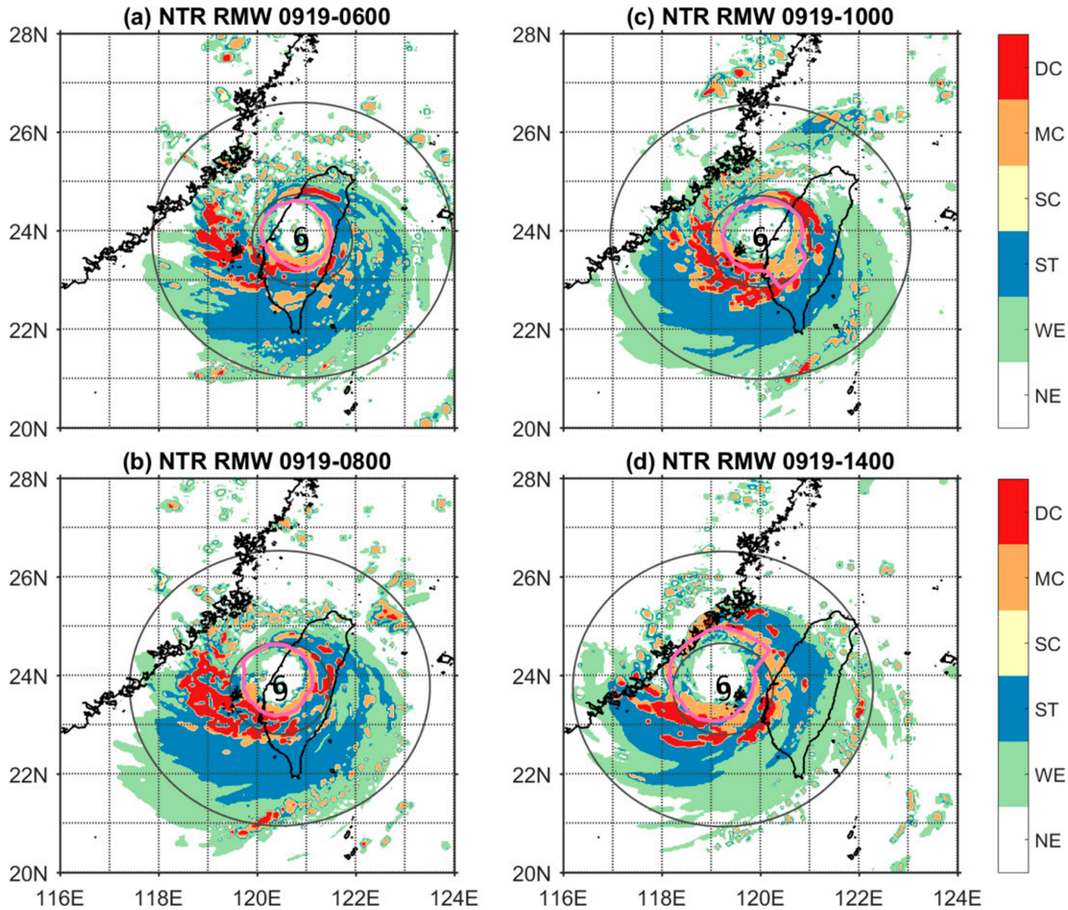

FIG. 5. As in Fig. 4, but for NTR experiment.

A buffer zone existed between the TC inner core and the radius of 1000 km; outside the buffer zone, all meteorological variables are the same as those in the CTL experiment. This NTW run started at 2100 UTC 18 September and ended at 0600 UTC 20 September 2010.

Figure 2a shows the best track analysis of Typhoon Fanapi from the Central Weather Bureau (CWB; black), and the simulated tracks from the CTL (red), NTR (blue), and NTW (orange) experiments. When Typhoon Fanapi approached the CMR, both the observed and the simulated CTL tracks had obvious southward deflections. In contrast, the NTR and NTW experiments showed east–west tracks with no obvious deflection, as expected if there were no mountains in Taiwan Island (Yeh and Elsberry, 1993a,b; Huang et al. 2011; Wu et al. 2015). The green triangles indicate the locations of the ground-based radars (RCCK, RCHL, RCMK, and RCCG) operated by the CWB and Republic of China Air Force (ROCAF), which provided the observed precipitation structures for TC Fanapi. The intensity of Fanapi became stronger in the absence of the CMR, as shown in NTR and NTW runs (Figs. 2b,c)

To classify different precipitation regimes, a convective–stratiform separation algorithm (Churchill and Houze 1984; Steiner et al. 1995; Yuter and Houze 1995; Didlake and Houze 2013a) is employed on the radar data at 2-km height. The separation technique is based on the radar reflectivity that exceeds a certain threshold ($Z_{bg} + \Delta Z_{cc}$ or 42 dBZ) determined by the background radar echo (Z_{bg}). The convective center criterion (ΔZ_{cc}), introduced by Yuter and Houze (1995), is shown in Eq. (1), where the coefficient $a = 9$ and $b = 45$ are taken from Didlake and Houze (2009). The convective radius (R; in units of kilometers) which depends on Z_{bg} is given by Eq. (2):

$$\Delta Z_{cc} = a\cos\left(\frac{1}{b}\,\frac{\pi Z_{bg}}{2}\right), \qquad (1)$$

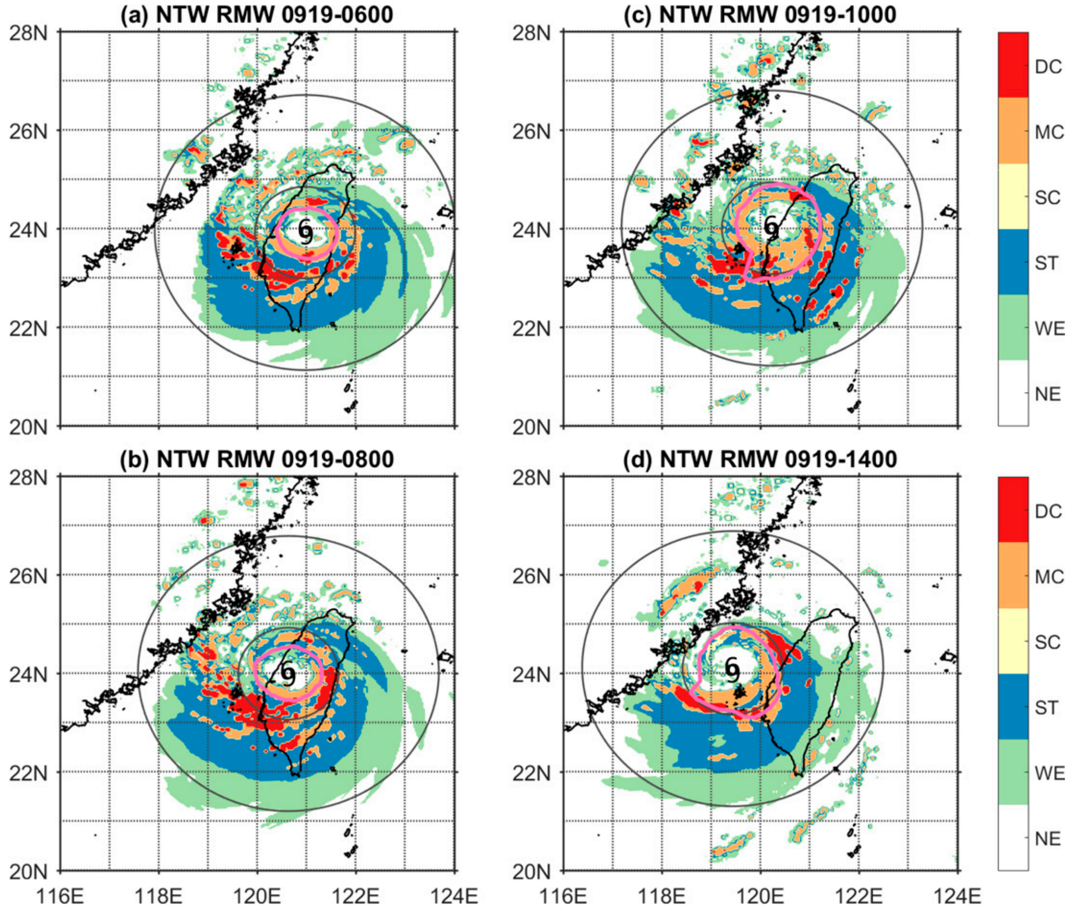

FIG. 6. As in Fig. 4, but for NTW experiment.

$$R = \begin{cases} 0.5, & Z_{bg} < 20\,\mathrm{dB}Z, \\ 0.5 + 3.5\left(\dfrac{Z_{bg} - 20}{15}\right), & 20 \le Z_{bg} < 35\,\mathrm{dB}Z, \\ 4, & Z_{bg} \ge 35\,\mathrm{dB}Z. \end{cases} \quad (2)$$

Following previous studies (Tao and Jiang 2015; Fritz et al. 2016; Rogers et al. 2020), the convective regions are further stratified into deep, moderate, and shallow convection. This stratification is based on the height of 20-dBZ echo top, with echo-top heights greater than 10 km classified as deep convection (DC), those with echo-top heights between 4 and 10 km classified as moderate convection (MC), and those with echo-top heights under 4 km classified as shallow convection (SC). In nonconvective regions, the areas with radar echo less than 20 dBZ are the weak-echo region (WE), and the areas with radar echo greater than 20 dBZ are the stratiform region (ST).

3. Precipitation regions of Typhoon Fanapi

Figure 3 shows the plan view of radar-observed (OBS) precipitation-regime classification at 2-km height using the convective–stratiform separation algorithm during the period when Typhoon Fanapi passed through the CMR. The reflectivity data from RCCK, RCHL, RCMK, RCCG, and RCKT radars are all included (see their locations in Fig. 2). Figure 3a shows the deep convection (DC) region scattered on the southwestern part of Taiwan at 0500 UTC. As Fanapi passed through the CMR, the percentage of deep convection increased in the southwest part of Taiwan (Fig. 3c at 1100 UTC) and later decreased after Fanapi moved into the Taiwan Strait (Fig. 3d at 1400 UTC). The moderate convection (MC) covered most of the radar-observed areas. The area between two rainbands was identified as stratiform precipitation. Note that the limited radar observed range was due to the algorithm that determined the precipitation type by reflectivity at 2-km height and echo-top height.

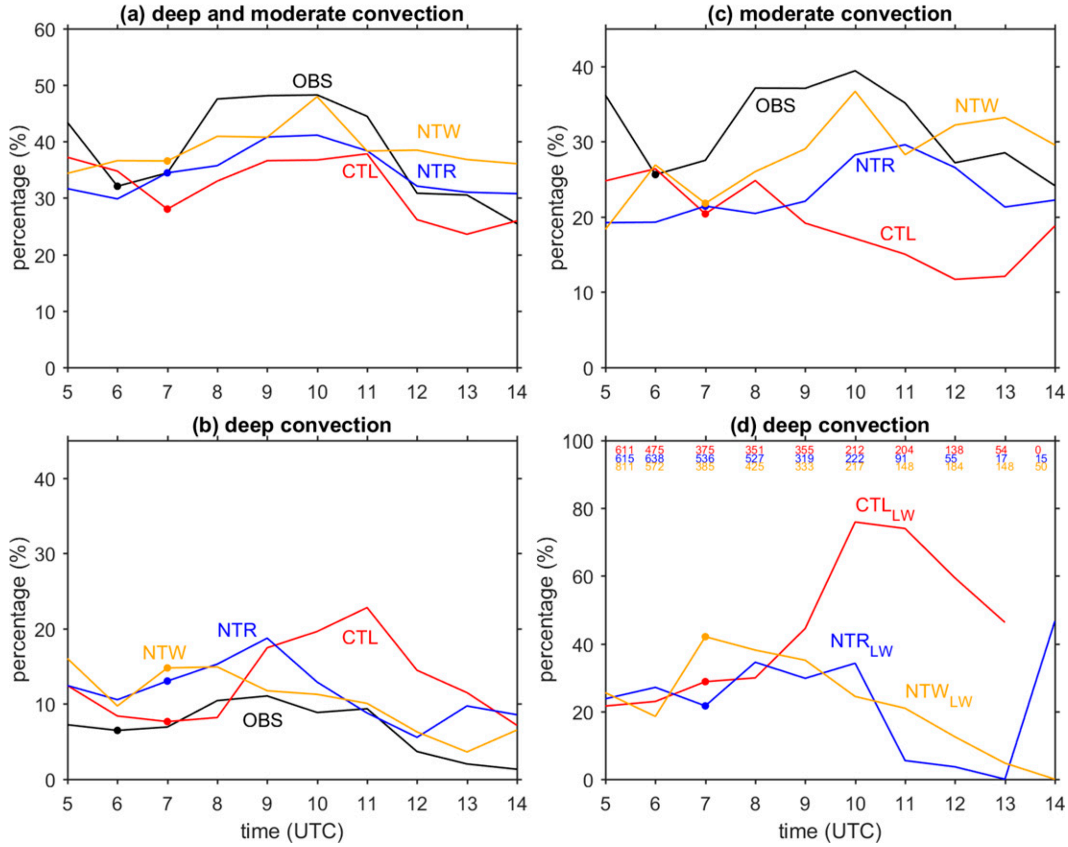

FIG. 7. The area percentages (%) of (a) deep convection (DC) and moderate convection (MC), (b) only deep convection (DC), and (c) only moderate convection (MC) within the inner core (with the radius less than 100 km) during the 8-h time period when TC Fanapi moved across the CMR. The dot along each curve indicates the time when the TC center is located at the foothill in the western slope of the CMR. (d) As in (b), but for the regions restricted to the area over land with the vertically averaged updrafts (from the surface to 12 km) greater than 0.5 m s^{-1}. Numbers at the top of (d) indicate number of grid points used in the calculation of area percentage at each hour.

Figure 4 shows the plan view of precipitation-regime classification at 2-km height from the CTL simulation using the convective–stratiform separation algorithm. Figures 5 and 6 present the corresponding results from the NTR and NTW simulations, respectively. The inner circles in Figs. 4, 5, and 6 indicate the radius of 100 km, and the outer circles indicate the radius of 300 km from the TC center. The CTL simulation shown in Fig. 4 captured the increase of deep convection

TABLE 1. The percentages of different precipitation regions from radar observation. Time T indicates the time when TC Fanapi's center left the CMR.

Time (UTC)	Time	Stratiform	No/weak echo	Shallow convection	Moderate convection	Deep convection
0500	$T - 1$ h	18.25	38.26	0.08	36.18	7.23
0600	T	17.74	49.35	0.82	25.62	6.48
0700	$T + 1$ h	21.89	42.68	0.97	27.52	6.93
0800	$T + 2$ h	20.24	31.21	0.99	37.12	10.44
0900	$T + 3$ h	17.48	32.48	1.90	37.09	11.06
1000	$T + 4$ h	23.82	26.94	0.96	39.42	8.86
1100	$T + 5$ h	19.73	34.83	0.94	35.14	9.36
1200	$T + 6$ h	14.85	52.81	1.47	27.19	3.67
1300	$T + 7$ h	8.17	59.54	1.74	28.52	2.02
1400	$T + 8$ h	6.02	68.09	0.42	24.15	1.32
Avg		16.82	43.62	1.03	31.80	6.74

TABLE 2. As in Table 1, but for the CTL experiment.

Time (UTC)	Time	Stratiform	No/weak echo	Shallow convection	Moderate convection	Deep convection
0500	$T-2$ h	37.52	24.56	0.68	24.79	12.44
0600	$T-1$ h	31.84	32.75	0.63	26.39	8.39
0700	T	29.47	42.23	0.26	20.40	7.65
0800	$T+1$ h	22.48	44.22	0.29	24.82	8.19
0900	$T+2$ h	20.00	43.22	0.14	19.17	17.46
1000	$T+3$ h	18.49	44.19	0.57	17.12	19.63
1100	$T+4$ h	20.09	41.74	0.34	15.04	22.80
1200	$T+5$ h	16.38	56.78	0.68	11.70	14.47
1300	$T+6$ h	16.58	58.23	1.60	12.10	11.50
1400	$T+7$ h	12.87	58.72	2.45	18.80	7.16
Avg		22.57	44.66	0.76	19.03	12.97

(DC) prior to and at the time when the center was re-emerging over water along the west coast of Taiwan Island (0800–1000 UTC), and the decrease of DC after the time when the center made "seafall" on the Taiwan Strait (1400 UTC). Note that the locations of the radius of maximum wind (RMW) are added in Fig. 4. Before the eyewall reorganization (0600 and 0800 UTC at Figs. 4a,b), most of the radar echoes with deep convection (DC) and moderate convection (MC) occurred outside the RMW. After the eyewall regeneration (at 1000 and 1400 UTC at Figs. 4c,d), more DC radar echoes occurred inside the RMW, indicating a higher heating efficiency for TC reintensification (Schubert and Hack 1982). Also note that the use of a different microphysics scheme affects the partition of precipitation regimes in Fig. 4. For example, another run with the WDM6 microphysics scheme produced excessive DC and insufficient MC and ST regimes (not shown). Because the CTL run with the Morrison scheme produced the precipitation structure in close resemblance to the observation [see Fig. 4c in Yang et al. (2018)], we use the CTL result in this study to discuss the vorticity budget. Note that although microphysics schemes keep improving, there are still some deficiencies in the parameterization.

The NTR experiment in Fig. 5, reflecting the absence of the CMR, displayed a more symmetric and organized distribution of deep convection (DC), moderate convection (MC), and stratiform (ST) before and after moving over the Taiwan Strait, compared to those in the CTL. The precipitation types in the CTL and NTR simulations showed that the convective cells are embedded within the inner-core rainbands, and the outer rainbands are mainly classified as stratiform and weak-echo region. Some studies documented that convective-scale features varied with radius in tropical cyclones (Corbosiero and Molinari 2002, 2003; Didlake and Houze 2013a,b). The stratiform region was located in the outer rainbands with ice particles injected from convective cells in the inner core. Powell (1990) and May (1996) proposed that the stratiform region containing active convective cells was different from the downwind stratiform region. The difference between stratiform regions with connected and separated convective cells is another interesting topic and should be examined carefully in future studies. The distribution of precipitation type in

TABLE 3. As in Table 1, but for the NTR experiment.

Time (UTC)	Time	Stratiform	No/weak echo	Shallow convection	Moderate convection	Deep convection
0500	$T-2$ h	33.92	32.55	1.85	19.23	12.44
0600	$T-1$ h	31.64	36.26	2.25	19.29	10.56
0700	T	25.16	38.97	1.40	21.43	13.04
0800	$T+1$ h	26.36	35.89	2.00	20.46	15.29
0900	$T+2$ h	23.97	32.72	2.48	22.08	18.74
1000	$T+3$ h	19.80	37.55	1.51	28.25	12.90
1100	$T+4$ h	20.86	38.29	2.48	29.59	8.79
1200	$T+5$ h	19.54	46.31	2.03	26.56	5.56
1300	$T+6$ h	15.35	49.64	3.97	21.31	9.73
1400	$T+7$ h	21.03	47.02	1.17	22.23	8.56
Avg		23.76	39.52	2.11	23.04	11.56

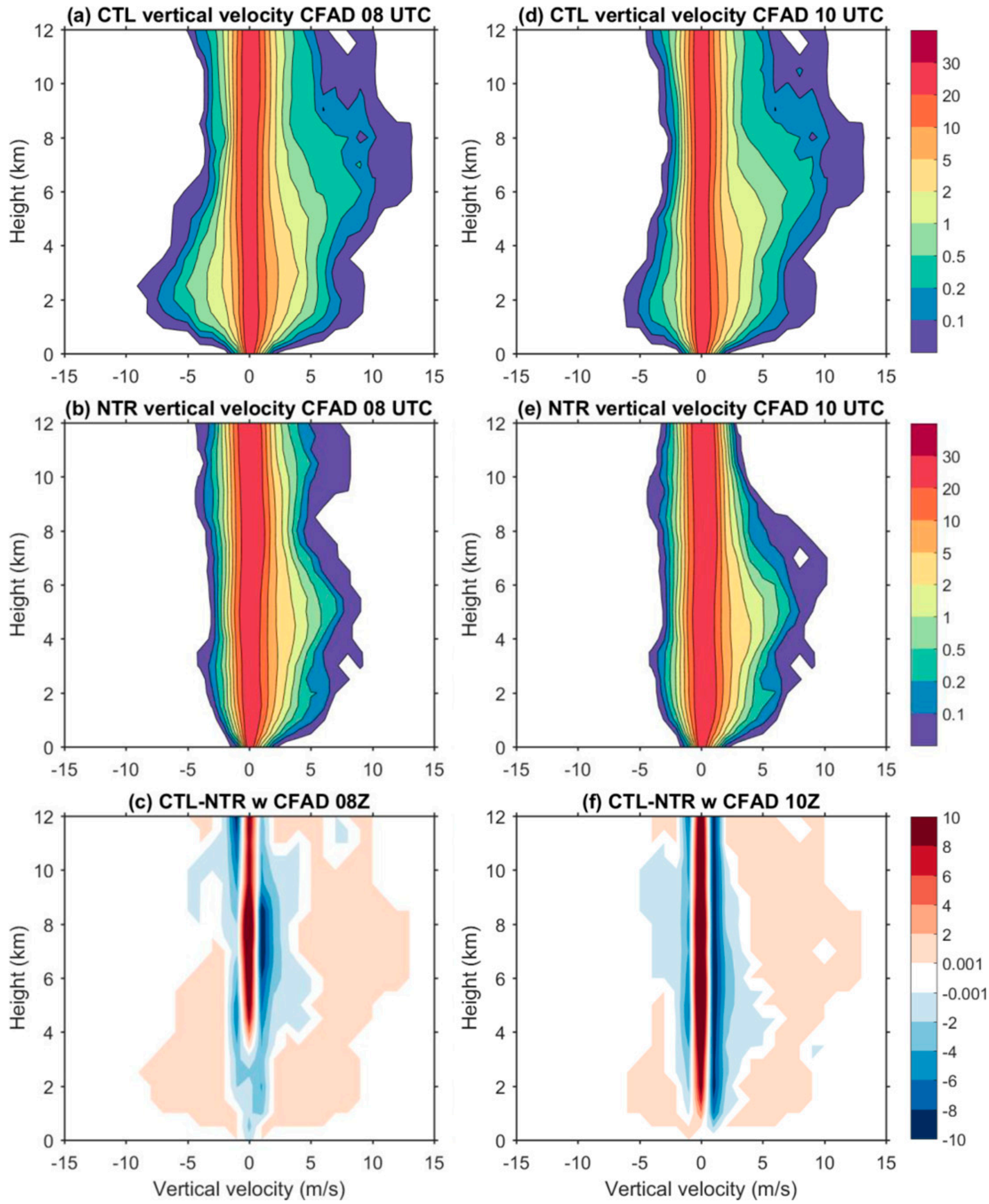

FIG. 8. Contoured frequency by altitude diagrams (CFAD; %) of vertical velocity within the TC inner core (with a radius less than 100 km) in (a),(d) CTL experiment; (b),(e) NTR experiment; and (c),(f) the difference between CTL and NTR experiments at (a)–(c) 0800 and at (d)–(f) 1000 UTC 19 Sep 2010.

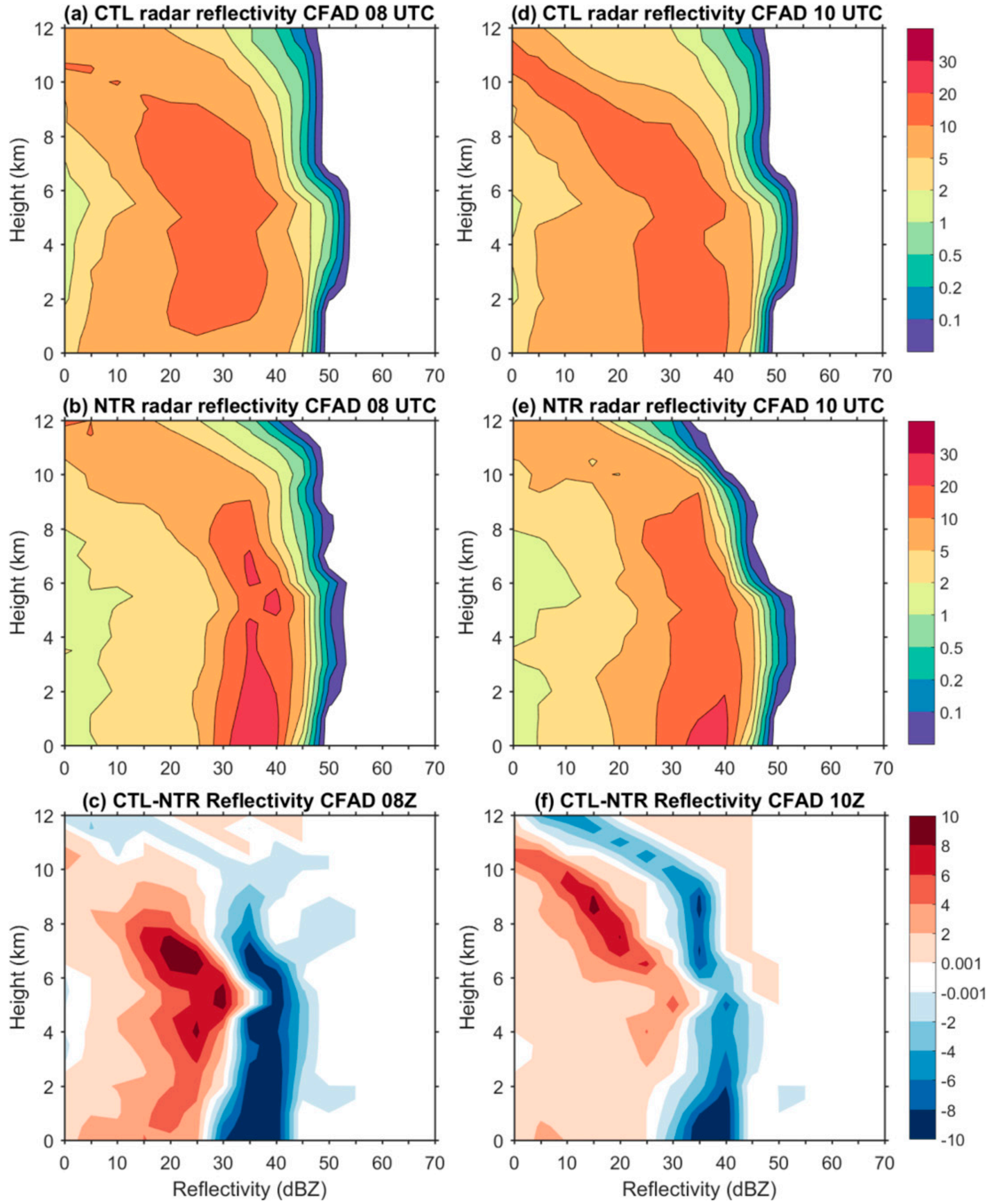

FIG. 9. As in Fig. 8, but for the CFAD of radar reflectivity.

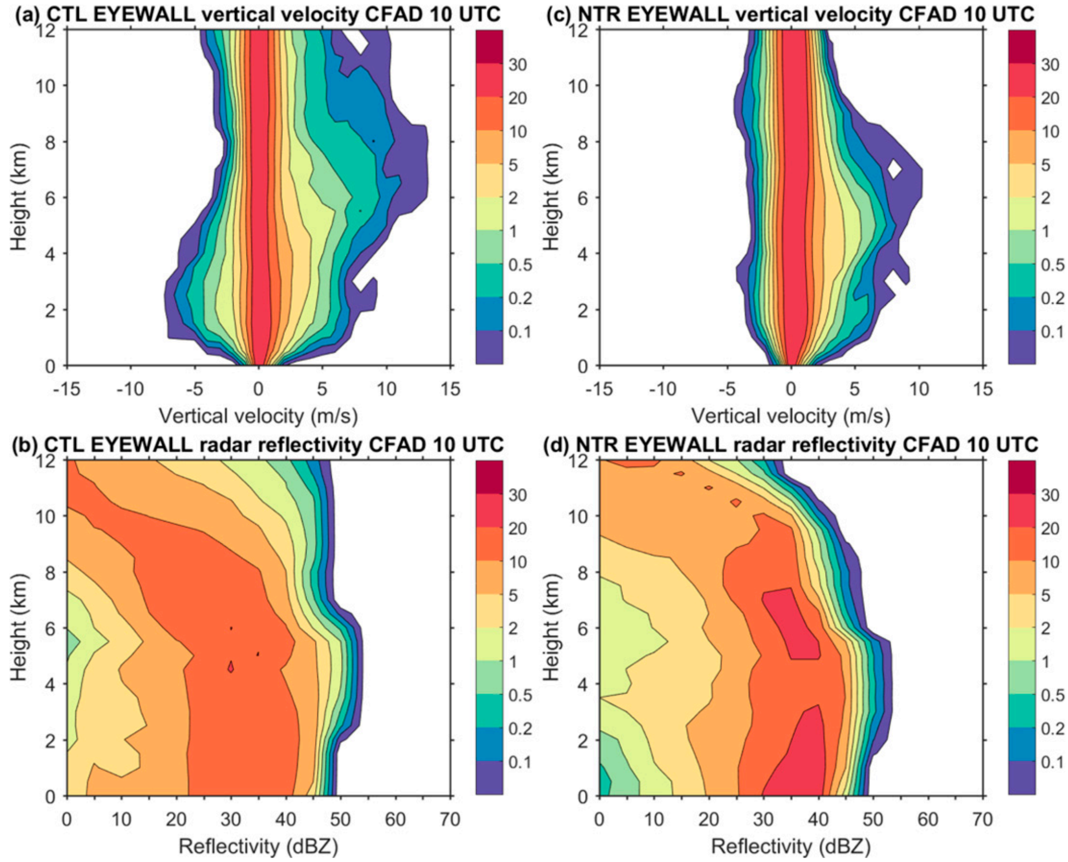

FIG. 10. CFAD of (top) vertical velocity and (bottom) radar reflectivity within the eyewall (with a radius between 50 and 100 km) in (a),(b) CTL experiment and (c),(d) NTR experiment at 1000 UTC 19 Sep 2010.

the NTW experiment (Fig. 6) is similar to that in the NTR experiment (Fig. 5), except for a smaller percentage of deep convection (DC) and a larger percentage of stratiform (ST) and weak-echo (WE) precipitation.

Figure 7 shows the time series of the relative proportion of (Fig. 7a) the summation of deep and moderate convection, (Fig. 7b) only deep convection, and (Fig. 7c) only moderate convection in the radar data from the observation (OBS), CTL, NTR, and NTW simulations within the TC inner core (with radius $\leq$ 100 km). Tables 1–3 show the detailed relative proportions of precipitation type in the OBS, CTL, and NTR, respectively. In Fig. 7a, both OBS and CTL show that the summation of DC and MC decreased before TC Fanapi passed through the CMR and then increased (from 30% to 50% in OBS and from 30% to 40% in CTL) afterward. In comparison with the radar OBS, the CTL simulation overproduced the percentage of deep convection and underproduced the percentage of moderate convection (Figs. 7b,c). These inconsistencies of deep and moderate convection between the radar observation and CTL simulation may have resulted from deep convective cells simulated in the numerical model that were too strong and wide compared to observations. Without the CMR, the NTR and NTW experiments had a greater occurrence of moderate convection (more than 20%) and a smaller occurrence of deep convection (less than 20%) during the 8-h time period.

Figure 8 shows the comparisons of contoured frequency by altitude diagrams (CFADs; Yuter and Houze 1995) of vertical velocity within the TC inner core (with radius $\leq$ 100 km) between the CTL and NTR experiments at 0800 and 1000 UTC. The downdrafts decreased in magnitude below 4-km altitude while the distribution of updrafts remained almost the same in the CTL experiment after TC Fanapi left the CMR at 1000 UTC (Figs. 8a,d). On the other hand, for the NTR storm, the downdrafts had little change but the strong updrafts (with vertical velocities > 5 m s^{-1}) were not able to reach altitudes of 10 km or higher (Figs. 8b,e). This fact indicates that convection within the inner core of TC Fanapi would weaken by 1000 UTC if the CMR were absent. The CTL storm at this time had more updrafts at upper levels

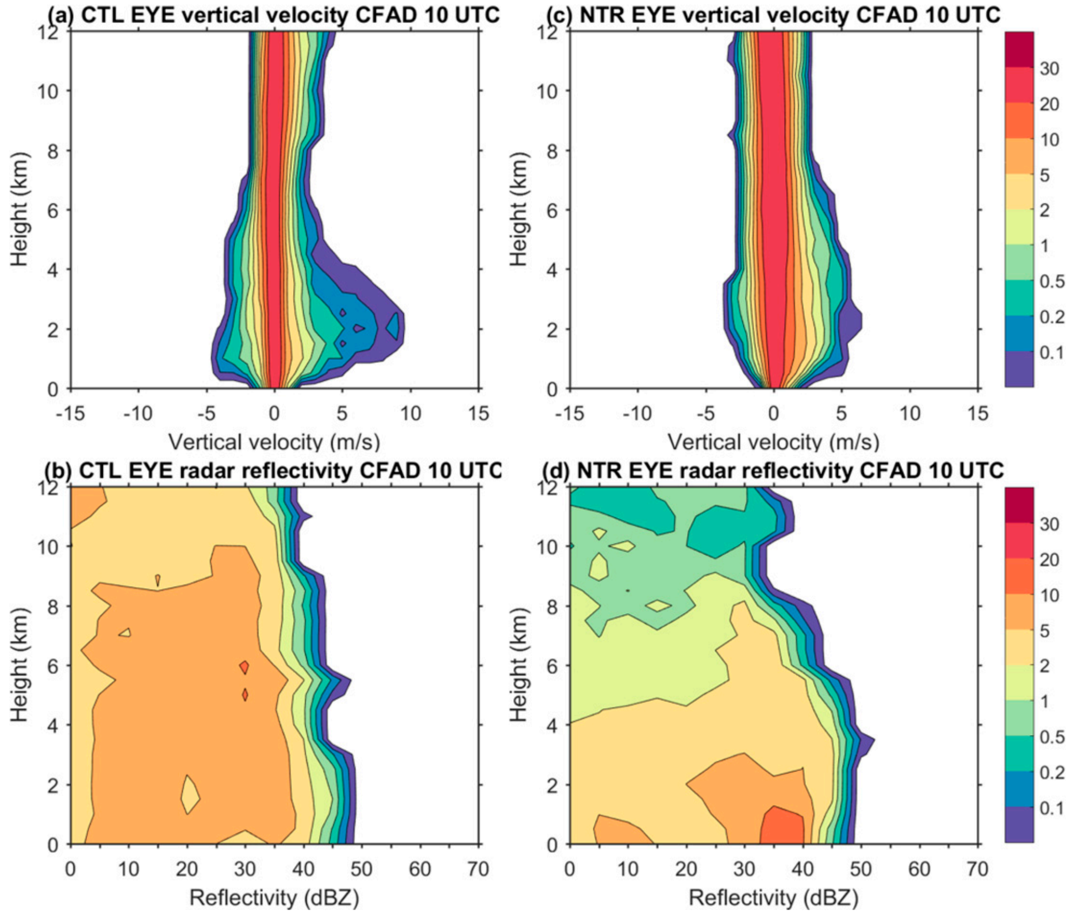

FIG. 11. As in Fig. 10, but for the eye region at 1000 UTC 19 Sep 2010.

(>6 km) and more downdrafts at lower levels (<4 km) than those in the NTR storm (Figs. 8c,f). This is consistent with Fig. 7d, which displays the statistics in the inner core but over land with terrain-forced ascent, that showed more deep convection occurring in the CTL at this time.

Figure 9 shows the comparisons of CFAD of radar reflectivity between the CTL and NTR experiments at 0800 and 1000 UTC. The CFAD in the CTL experiment had an increasingly diagonal slope of the mode above 6-km altitude after Fanapi had moved across the CMR and was exiting Taiwan Island (Figs. 9a,d). The CFAD in the CTL simulation showed more convective characteristics with higher percentage of strong echo (30–40 dBZ) below 1 km at 1000 UTC. Without the CMR, the frequency of strong radar echoes (30–40 dBZ) decreased at the middle levels (4–8 km) in the NTR storm due to the weakening of Typhoon Fanapi (Figs. 9b,e). Over most altitudes (below 10 km), the CTL storm had more weak echoes (<25 dBZ) and fewer stronger echoes (25–45 dBZ) than those in the NTR storm (Figs. 9c,f). Above 10-km altitude, however, the CTL storm had more strong radar echoes (>40 dBZ) than the NTR (Fig. 9f) at 1000 UTC; this high-reflectivity values at upper level could be a flaw from the microphysics scheme (Hence and Houze 2011).

After looking at the CFAD profiles averaged within the whole inner core, now we can examine the CFAD profiles representing several subregions (e.g., eyewall vs eye regions and deep convection vs moderate convection regions). It is clear from Figs. 10a and 10c that at 1000 UTC within the eyewall region ($50 < r < 100$ km), the CTL experiment displayed a higher percentage of updrafts at upper levels (6–10 km) and downdrafts at lower levels (below 4 km), compared to the NTR experiment. On the other hand, the NTR experiment had a higher percentage of medium-strength radar echoes of 30–40 dBZ than the CTL experiment (Figs. 10c,d). For the eye region ($r < 50$ km) at 1000 UTC, the CTL experiment displayed a greater population of strong updrafts (with peak intensity up to 10 m s^{-1}) at lower levels (below 4 km) than those in the NTR experiment (Figs. 11a,c), but the NTR run had a larger percentage of medium-strength radar echoes of 30–40 dBZ at lower levels (below 2 km) than those in the CTL (Figs. 11b,d).

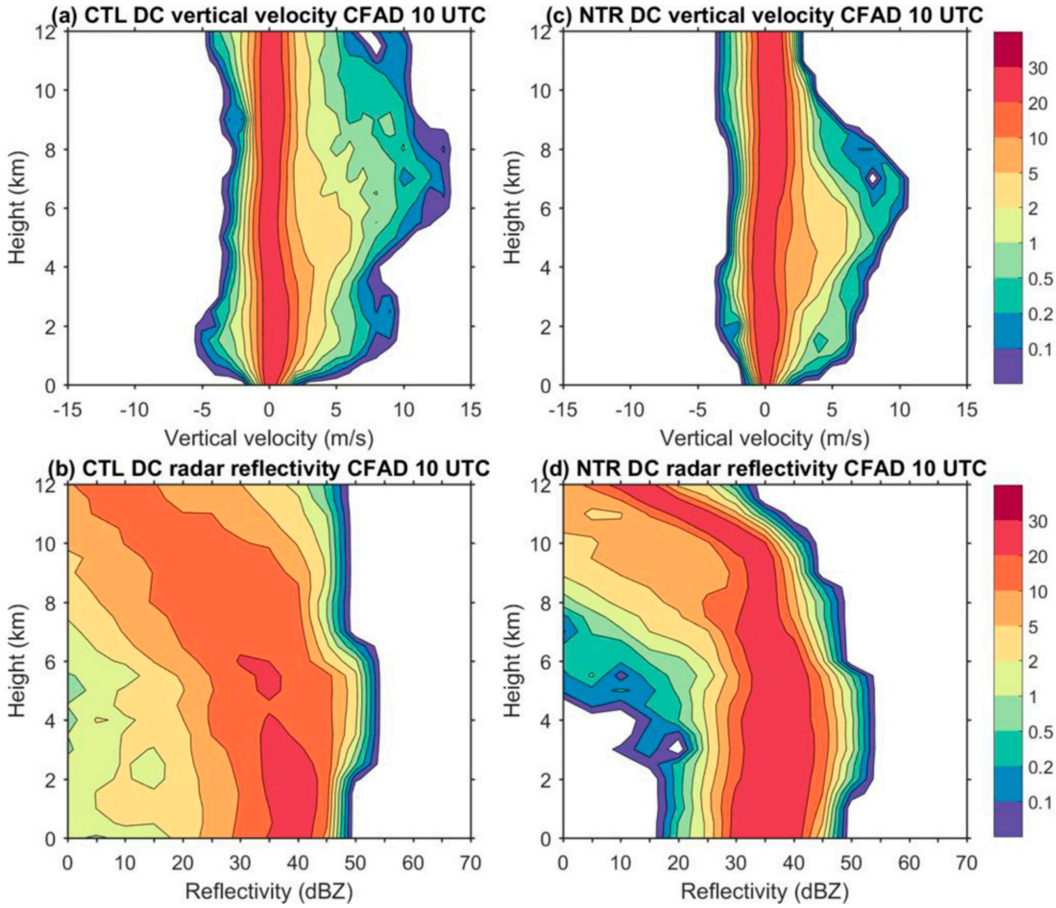

FIG. 12. CFAD of (top) vertical velocity and (bottom) radar reflectivity within the deep convection (DC) region in (a),(b) the CTL experiment and (c),(d) the NTR experiment at 1000 UTC 19 Sep 2010.

Now let us compare the CFAD profiles between the deep convection (DC) and moderate convection (MC) regions. For the DC region at 1000 UTC, the CTL experiment displayed a higher percentage of updrafts at upper levels (6–10 km) and downdrafts at lower levels (below 4 km) than those in the NTR experiment (Figs. 12a,c). For the radar reflectivity field in the DC region (Figs. 12b,d), the NTR experiment had a higher percentage of medium-strength radar echoes of 30–40 dB*Z*. Similarly, for the moderate convection (MC) region at 1000 UTC, the CTL run displayed a higher percentage of updrafts at middle levels (4–8 km) and downdrafts at lower levels (below 4 km) than those in the NTR experiment (Figs. 13a,c). For radar reflectivity CFAD profiles, the CTL run had a similar profile to that of the NTR (Figs. 13b,d).

The comparison of vertical profiles of mean environmental conditions inside the TC inner core (within a 100-km radius) between the CTL and NTR experiments is displayed in Fig. 14. Figures 14a and 14d illustrate the vertical profiles of relative humidity (RH) in the CTL and NTR storms, respectively. It is shown that the inner core was much drier in the CTL, due to strong subsidence on the lee side of the CMR. When Fanapi's inner core moved into Taiwan, evaporation from falling hydrometeors cooled the air and added to the forced descent on the lee side of the CMR, and the subsidence drying dominated over the moistening from evaporation. Figures 14b and 14e show a comparison of the vertical profiles of mean temperature anomaly (departure from the area mean) within the inner core ($r \leq 100$ km) between the CTL and NTR experiments. The positive temperature anomaly occurred at lower levels (below 4-km height) at 0700 UTC as the strong TC circulation hit the CMR, inducing deep convection to develop and increasing temperature anomaly by strong latent heat release (Fig. 14b). On the other hand, the negative temperature anomaly in the NTR experiment resulted from the evaporative cooling induced by precipitation.

Figures 14c and 14f show the comparison of the vertical profiles of mean equivalent potential temperature (θ_e; solid line) and saturated equivalent potential temperature (θ_{es}; dashed line) inside the inner core ($r \leq 100$ km) between the CTL and NTR experiments. The inner core of the CTL storm

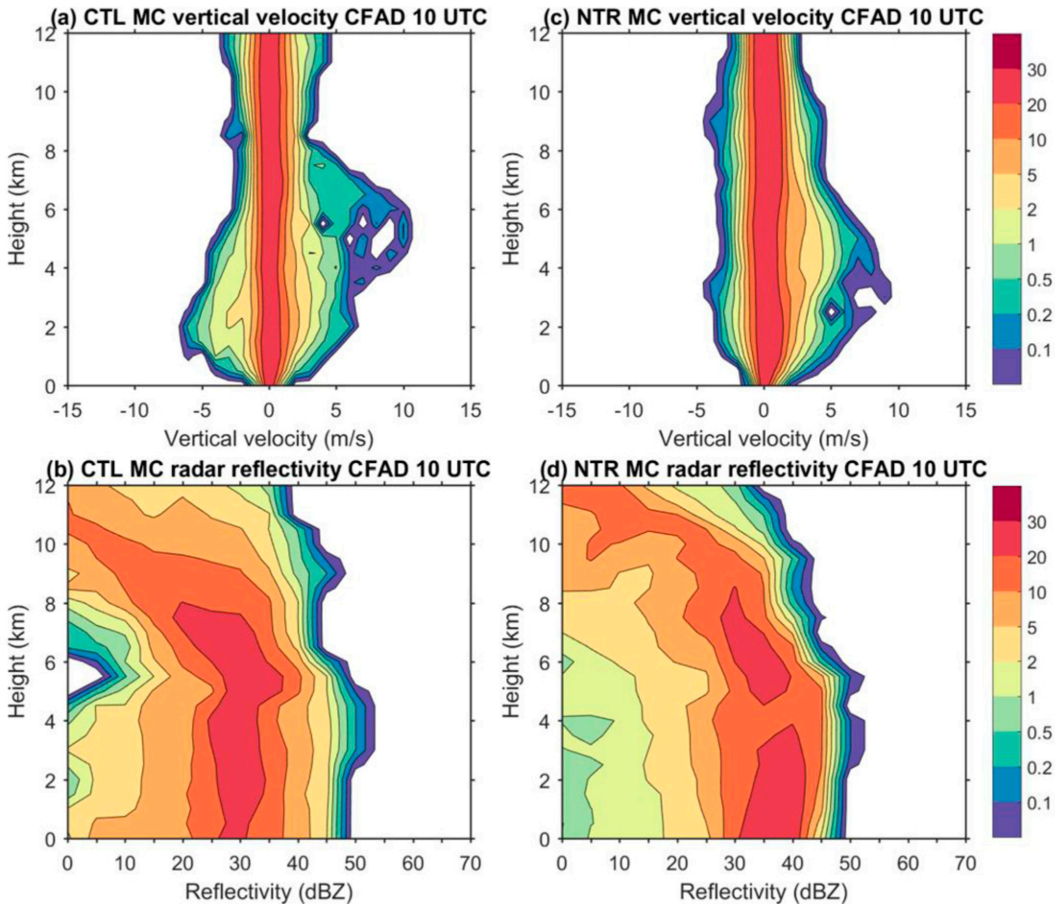

FIG. 13. As in Fig. 11, but for the moderate convection (MC) region.

at lower levels was more potentially unstable and much drier than that in the NTR storm. Therefore, the CTL storm had more deep convection, while the NTR storm had more moderate convection. Similar enhancement of deep convection in the TC inner core over the rugged terrain is also found in Geerts et al. (2000) for Hurricane Georges (1998; see their Figs. 7 and 10). This relationship between stability and humidity profiles and the prevalence of deep convection for Typhoon Fanapi (2010) with a drier lower troposphere, primarily due to terrain and evaporation-induced subsidence, was different from the analysis results of Hurricane Hermine (2016), which featured a tropical cyclone in persistent vertical shear over the open ocean, with no terrain interactions and a drier middle and upper troposphere (Rogers et al. 2020).

Figure 15 shows the comparison of the thermodynamic profiles between the eye and eyewall region at 1000 UTC. For the CTL experiment, the eye region is drier, has a stronger upper-level warm anomaly, and a shallower potentially unstable layer than those in the eyewall region. In the absence of the terrain effect (NTR experiment), the eye region is much drier above 4 km than the eyewall region, the eye region has a stronger warming in the troposphere (below 12 km) than the eyewall region, and the eye region has a deeper potentially stable layer at low levels than the eyewall region. These differences in thermodynamic profiles between the eye and eyewall region are associated with the differences in convection and precipitation (Figs. 10 and 11).

For the CTL simulation, the subsidence occurred when Typhoon Fanapi moved across the CMR. The primary rainband was established in the southern part of the TC (Figs. 4c and 16b). The relative humidity increased in the low levels due to precipitation evaporation. Terrain over the CMR enhanced the updrafts on the windward side and the thermodynamically unstable environment made the deep convection stronger and more prevalent (Figs. 7b and 16a). However, for the NTR experiment, the absence of extra water vapor supply at lower levels and less thermodynamically unstable environment led to the dominance of moderate convection (Fig. 7c).

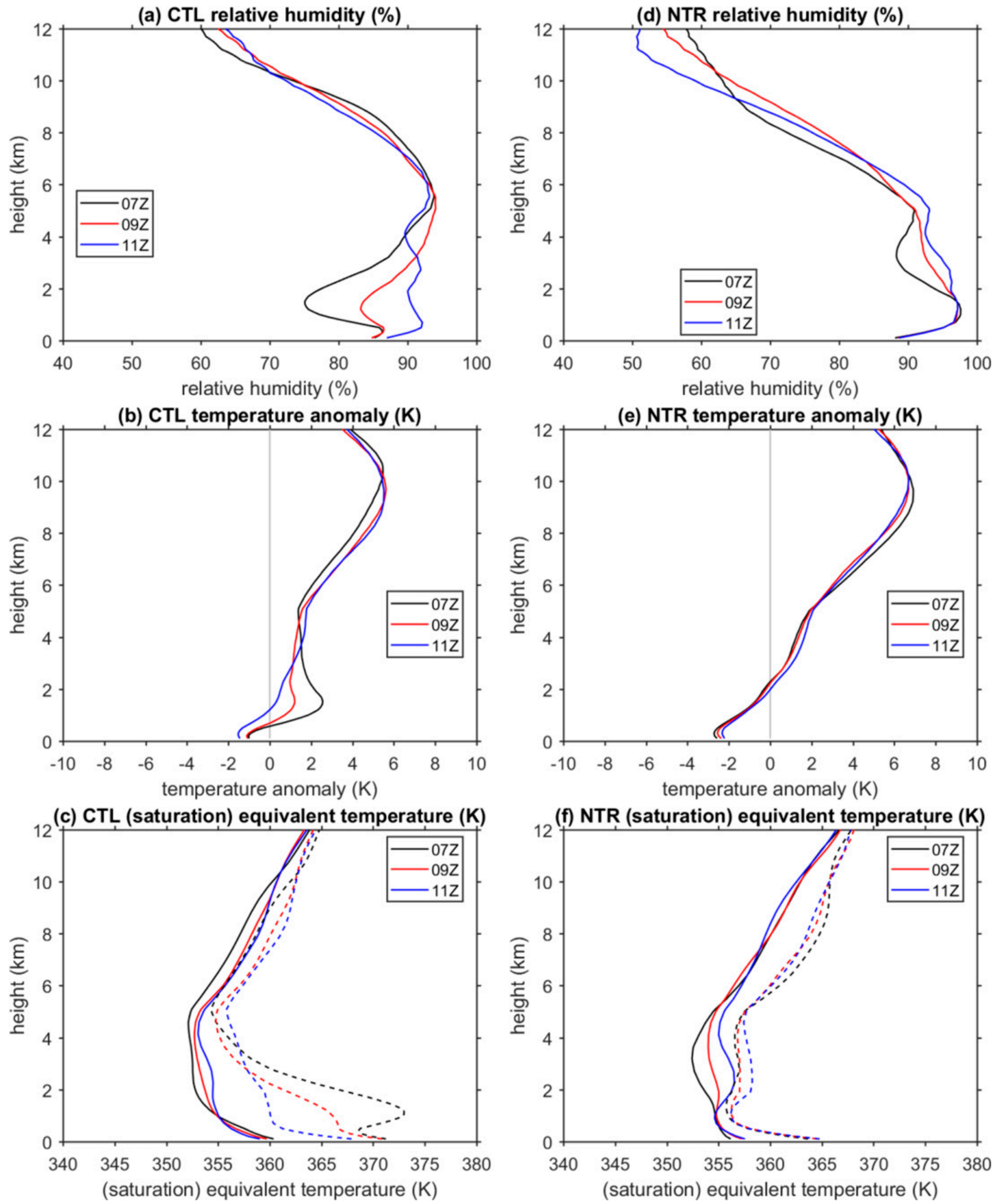

FIG. 14. The mean profiles of (a),(d) relative humidity (%); (b),(e) temperature anomaly (K); and (c),(f) equivalent potential temperature (K; solid line) and saturation equivalent potential temperature (K; dashed line) within the inner core (with a radius less than 100 km) in (a)–(c) the CTL experiment and (d)–(f) the NTR experiment at 0700 (black), 0900 (red), and 1100 UTC (blue) 19 Sep 2010.

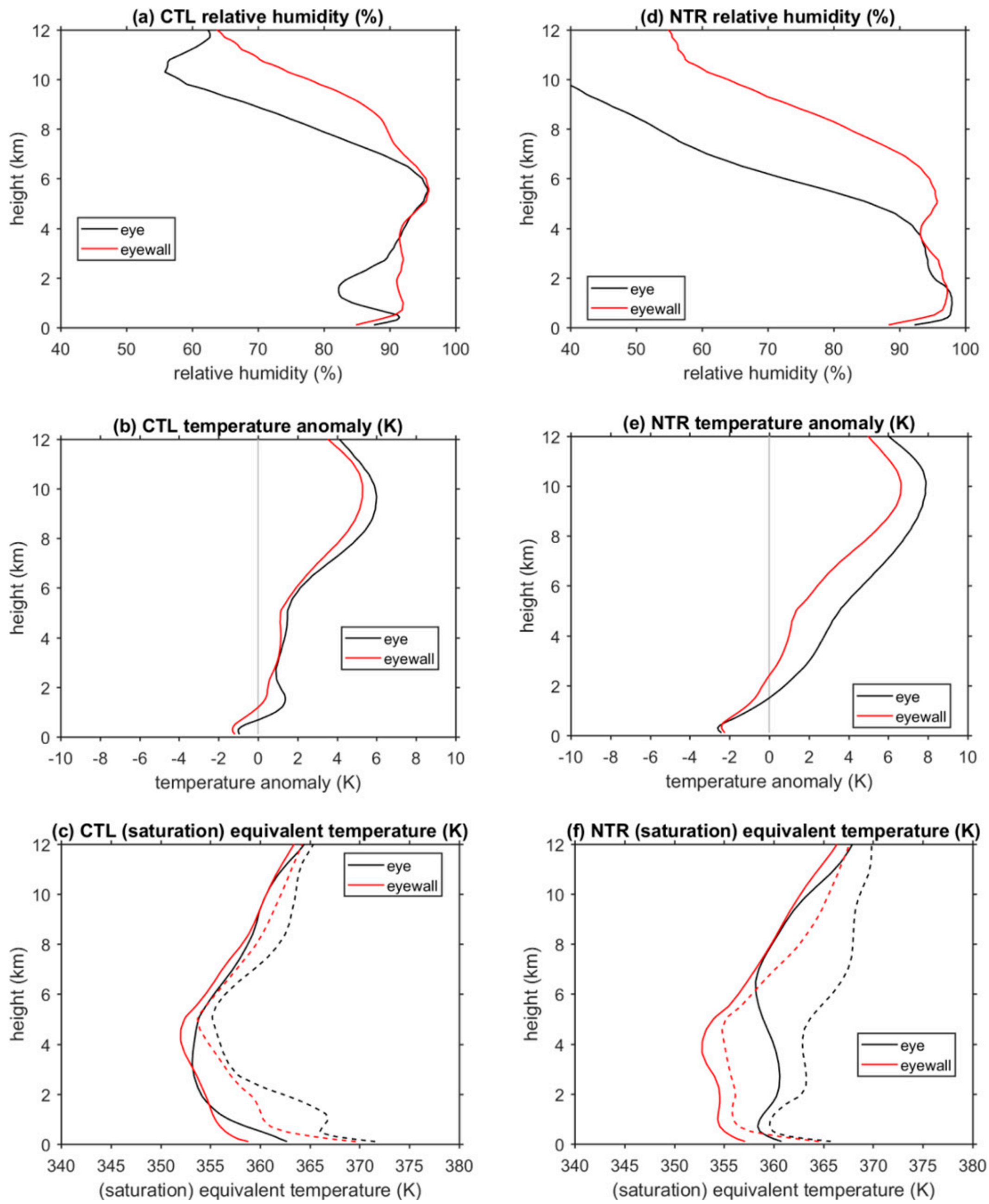

FIG. 15. The mean profiles of (a),(d) relative humidity (%); (b),(e) temperature anomaly (K); and (c),(f) equivalent potential temperature (K; solid line) and saturation equivalent potential temperature (K; dashed line) within the eye (with a radius less than 50 km) and eyewall (with a radius between 50 and 100 km) regions in (a)–(c) the CTL experiment and (d)–(f) the NTR experiment at 1000 UTC 19 Sep 2010.

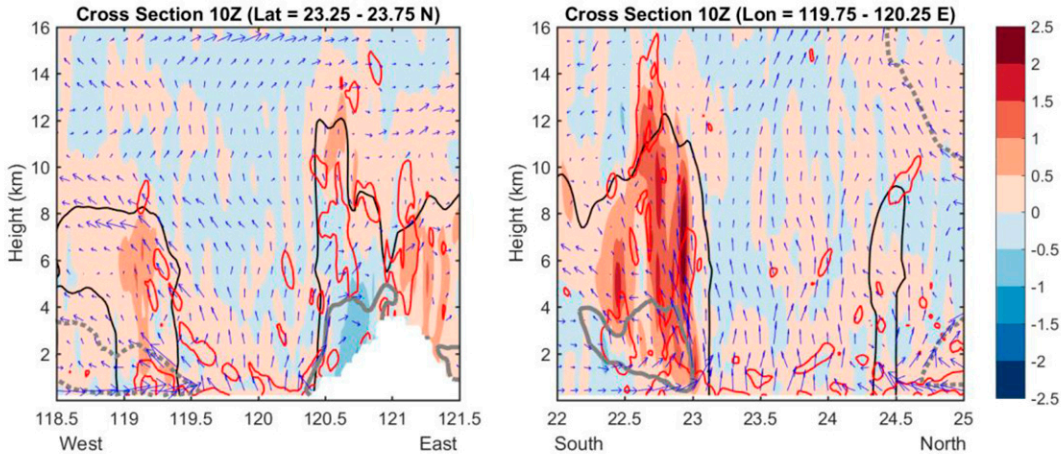

FIG. 16. The storm structure of the CTL storm at 1000 UTC: (a) zonal and (b) meridional cross sections of vertical velocity (colored), radar reflectivity contours of 20 dBZ (black), horizontal wind speed contours of 30 m s^{-1} (gray), stretching contours of 10^{-7} s^{-2} (red), and vorticity vectors along the cross section (blue). Each cross section is averaged with a 0.5° width. The horizontal locations of two vertical cross sections are displayed in Fig. 4c.

4. Vorticity budget analysis

Following Yang et al. (2018), a vorticity-budget analysis is employed in this study to examine the vorticity tendencies contributed by different precipitation regimes in the inner core of Typhoon Fanapi during its eyewall reorganization period. The vorticity budget equation in a TC center-following framework can be written as

$$\frac{\partial \zeta}{\partial t} + (\mathbf{V} - \mathbf{C}) \cdot \nabla \zeta + w\frac{\partial \zeta}{\partial z} = -\zeta(\nabla \cdot \mathbf{V}) - \left(\frac{\partial w}{\partial x}\frac{\partial v}{\partial z} - \frac{\partial w}{\partial y}\frac{\partial u}{\partial z}\right), \tag{3}$$

or

$$\mathrm{TND} + \mathrm{HAD} + \mathrm{VAD} = \mathrm{STR} + \mathrm{TIL}. \tag{4}$$

The variable ζ is the vertical relative vorticity and $\mathbf{C}$ is the TC translation vector. The terms on the left-hand side of Eq. (3) are local vorticity tendency (TND), horizontal advection (HAD), vertical advection (VAD), respectively. Terms on the right-hand side of Eq. (3) are stretching (STR), and tilting (TIL), respectively. It is clear from Eqs. (3) and (4) that redistribution of the three-dimensional vorticity is determined by the combination of HAD and VAD. The generation or consumption of vorticity is controlled by the STR and TIL.

Figure 17 displays the vertical structure of vertical relative vorticity, the summation of STR and TIL, and the vorticity tendency. For the CTL, Fanapi's vorticity decreased as a result of the weakening of the vortex circulation by the obstruction of the CMR (Fig. 17a). Later, more positive vorticity was formed by the STR and TIL forcings at lower levels (Figs. 17b,c). There is a layer of anticyclonic tendency above the cyclonic tendency near 1 km, and it is produced by the upward transport of anticyclonic vorticity generated by moderate convection. The westward tilt of the axis of vorticity is evident in Fig. 17b; the area with vorticity greater than 60×10^{-5} s^{-1} reached upward from 0600 to 1000 UTC, a clear indication of the bottom-up process. On the other hand, the vorticity structure was upright and remained compact from lower to middle levels in the NTR simulation (Figs. 17d–f).

To analyze how the vorticity forcings from the STR and TIL in different precipitation regions affected the reconstruction of Typhoon Fanapi's eyewall, contributions in different subregions were taken into account. According to Stokes's theorem, vorticity tendency contributions from different precipitation regimes can be expressed as circulation tendencies. Mathematically, for a horizontal wind vector $\mathbf{V}$, the circulation of $\mathbf{V}$ along a closed contour C can be expressed as

$$\oint_C \mathbf{V} \cdot d\mathbf{l} = \int\int_A (\nabla \times \mathbf{V}) \cdot \hat{\mathbf{k}}\, dA, \tag{5}$$

or

$$\delta C = \zeta \delta A, \tag{6}$$

where A is the horizontal area enclosed by the contour C, and $\hat{\mathbf{k}}$ is a unit vertical vector to the area element dA (Holton 2004). Thus, Stokes's theorem states that the circulation (δC) about any closed loop C is equal to the integral of the vertical component of the vorticity (ζ) over the area (δA) enclosed by the loop C, as indicated by Eq. (6).

Figures 18a and 18b show the vertical profiles of circulation tendency from the STR within the convective region (CV),

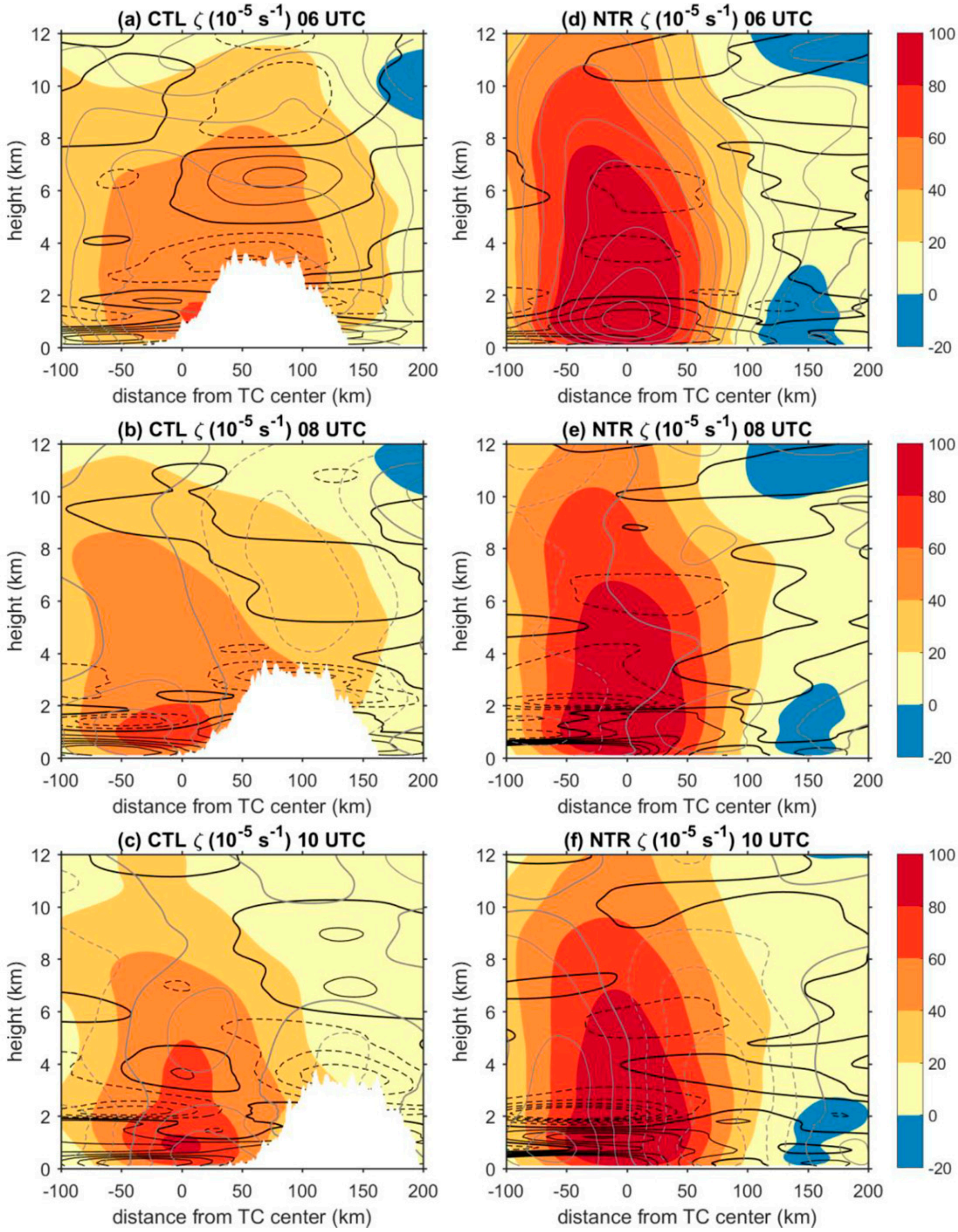

FIG. 17. The vertical structure of vorticity (10^{-5} s^{-1}; colored), the summation of STR and TIL terms (s^{-2}; solid black line for cyclonic tendency and dashed black line for anticyclonic tendency), and vorticity tendency (TEN; s^{-2}; solid gray line for cyclonic tendency and dashed gray line for anticyclonic tendency). (a)–(c) CTL experiment and (d)–(f) NTR experiment. All fields with physical scales smaller than 200 km are filtered out, and an average for 200 km in the north–south direction is applied.

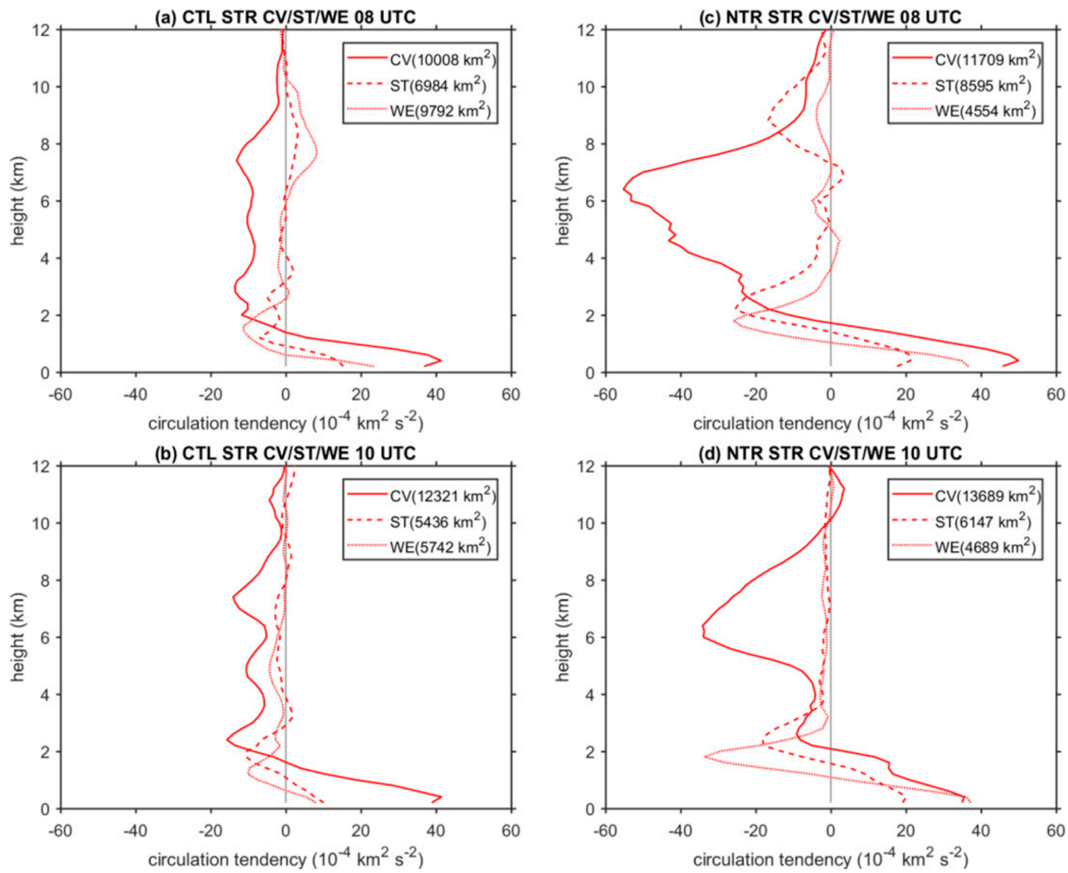

FIG. 18. The vertical profiles of circulation tendency (10^{-4} km^2 s^{-2}) for the STR term. The solid line indicates the contribution by the convective region (CV), the dashed line is for the stratiform region (ST), and the dotted line is for the weak- and no-echo region (WE). (a),(b) CTL experiment and (c),(d) NTR experiment. Times are (a),(c) 0800 and (b),(d) 1000 UTC 19 Sep 2010. Note that the size of each region is indicated in the panel legends; for example, the size of convective region (CV) at 0800 UTC is 10 008 km^2.

stratiform region (ST), and weak or no echo region (WE) in the CTL at 0800 and 1000 UTC, respectively. At lower levels, the STR in the convective region remained dominant, compared to those in other precipitation regimes (Fig. 18a). When Typhoon Fanapi underwent an eyewall reorganization process (at 1000 UTC), the STR in the convective region remained dominant at lower levels, but the STR in the stratiform and weak-echo regions became smaller (Fig. 18b). For the NTR experiment, the STR in the CV region became weaker from 0800 to 1000 UTC (Figs. 18c,d).

Figure 19 displays the vertical profiles of circulation tendency from the TIL within the convective region (CV), stratiform region (ST), and weak or no echo region (WE) in the CTL and NTR simulations. In the CTL, the TIL in convective region became more positive in lower levels and oscillated in the vertical at 1000 UTC (Figs. 19a,b). In the absence of CMR, the TIL in the convective region oscillated in the vertical with a slight weakening (Figs. 19c,d). Despite the TIL within the convective region being positive in the middle levels (3–6-km height), the negative STR within the convective region canceled out the cyclonic contribution in the NTR (Figs. 18c and 19c). Note that the increase of tangential wind in the CTL experiment as the eyewall reorganized would increase vertical wind shear in the boundary layer such that the TIL became more positive in lower levels as the TC intensity increased and its eyewall was reorganized.

Figure 20 shows the circulation tendency from the STR and TIL terms in deep convection and moderate convection regions. At 0800 UTC, the low-level STR and TIL in the moderate convection region was greater than those in the deep convection region in both CTL and NTR experiments (Figs. 20a,c). Later at 1000 UTC, the STR in deep convection became stronger in the CTL experiment (with the CMR terrain) but remained secondary in NTR (without terrain). In

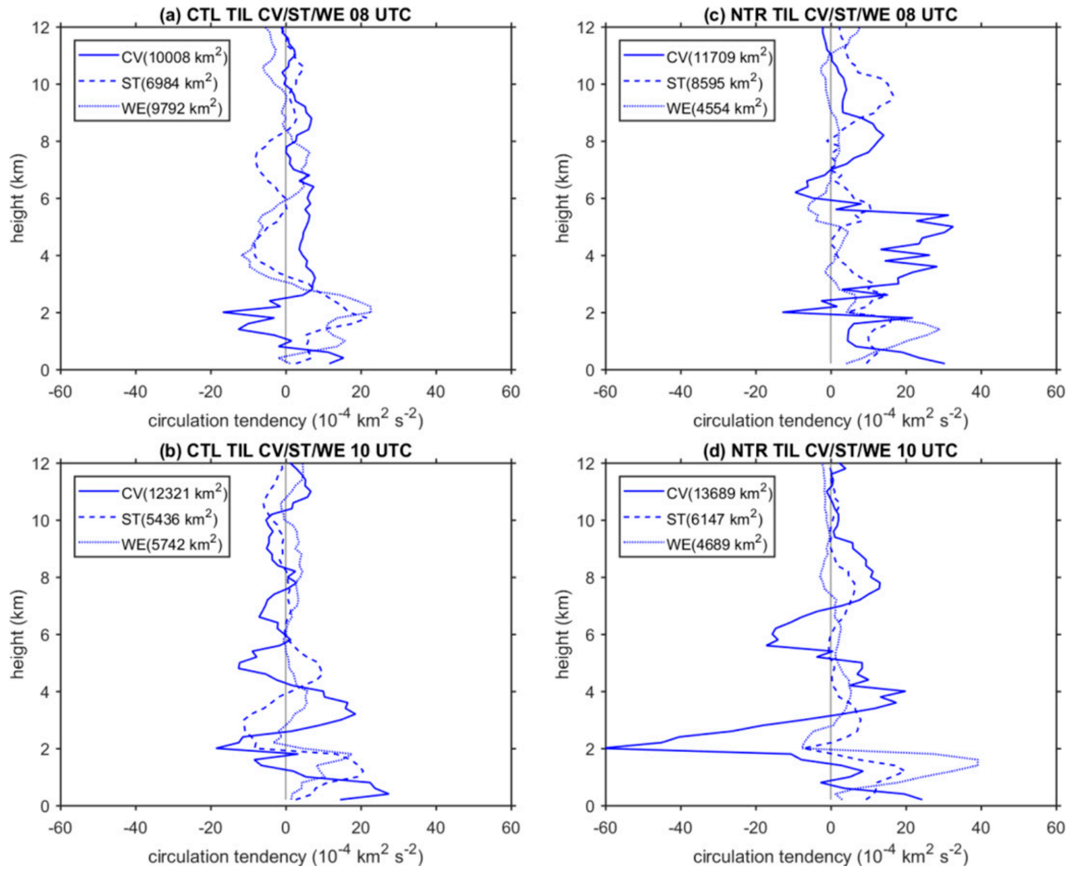

FIG. 19. As in Fig. 18, but for the vertical profile of circulation tendency for the TIL term.

the CTL experiment, the STR and TIL in the deep convection region increased, as a result of the decrease of moderate convection and the increase of deep convection (Figs. 7b,c). This indicated the terrain forcing in the deep convection region coupled with a drier and more unstable environment for the CTL simulation (Figs. 14a,c), compared to the NTR experiment. From the comparison of Figs. 18c and 20c, it indicates that the stronger negative circulation tendency in the middle levels is because of the wider area of divergence over the convective region with both deep and moderate convection.

Because the NTR experiment had a stronger TC vortex circulation and more intense convection without the disruption by the CMR, this might enhance the upward transport of positive vorticity by strong convection. A no-terrain-weak (NTW) experiment with a warmer, drier, and weaker TC inner core is conducted, with the experiment setup described in section 2. This NTW run has a track very similar to the NTR track (Fig. 2a) and its intensity is between those of the CTL and NTR experiments (Figs. 2b,c). For this NTW experiment, the STR in the convective region is dominant (compared to stratiform ST and weak-echo WE regions) and produces a positive vorticity tendency at low levels (below 2 km), as displayed in Fig. 21a. The TIL in the convective region is also dominant and produces negative vorticity at middle levels (2–4 km; Fig. 21b). If the vorticity forcing is decomposed into deep convection (DC) and moderate convection (MC) components, then the positive vorticity of the STR term at low levels (below 2 km) and negative vorticity of the TIL term at middle levels (2–4 km) are mainly determined by the MC component (Fig. 21c). These results are similar to those in the NTR experiment (see Figs. 18d, 19d, and 20d), albeit with different magnitudes. Thus for the similar vorticity-budget balances between the NTW and NTR experiments, it is implied that the NTR experiment is still relevant in determining the vortex stretching in convection, even without the flow modification by the CMR.

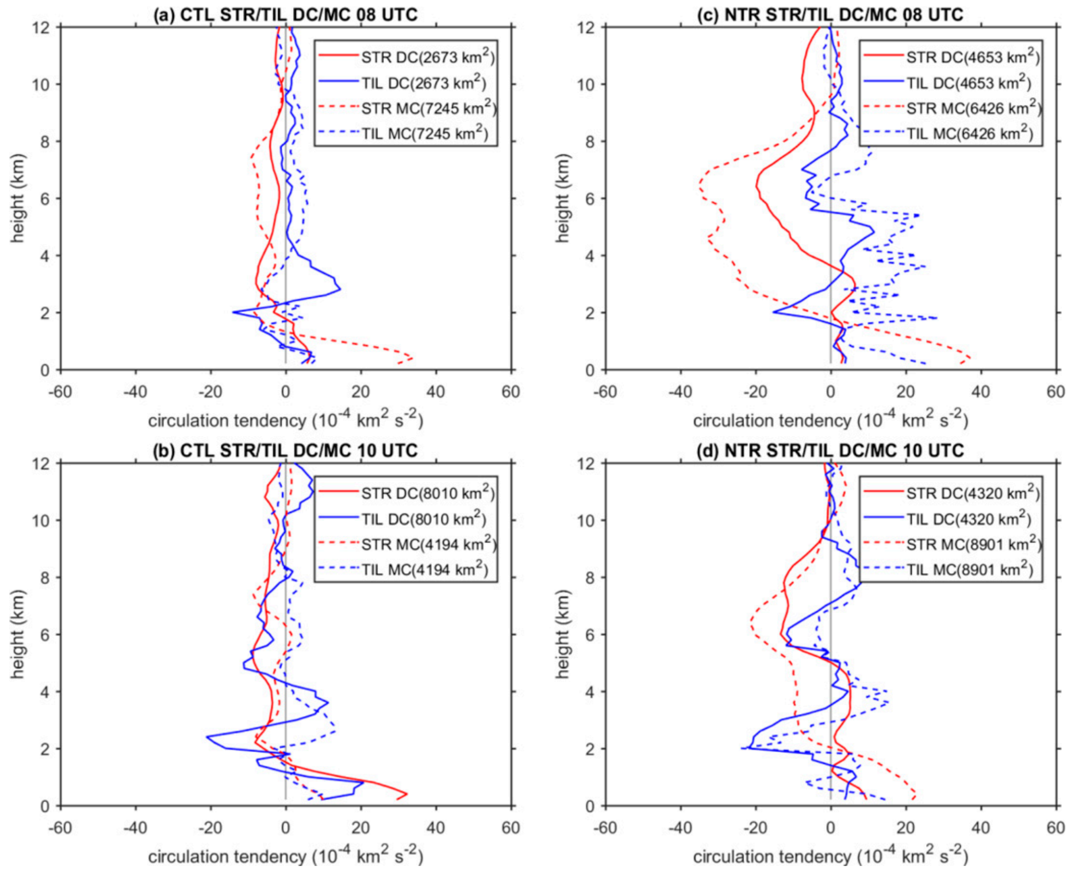

FIG. 20. The vertical profiles of circulation tendency (10^{-4} km^2 s^{-2}) from (a),(b) CTL experiment and (c),(d) NTR experiment. The solid red line indicates the stretching term in deep convection (STR DC), the solid blue line indicates the tilting term in deep convection (TIL DC), the red dashed line indicates the stretching term in moderate convection (STR MC), and the blue dashed line indicates the tilting term in moderate convection (TIL MC). (a),(c) 0800 and (b),(d) 1000 UTC 19 Sep 2010. Note that the size of each region is indicated in the panel legends; for example, the size of deep convection region (DC) at 0800 UTC is 2673 km^2.

Recall the storm structure at 1000 UTC to the west of the CMR as shown in the zonal and meridional cross sections of vertical velocity, radar reflectivity, horizontal wind, and vorticity vectors in Fig. 16. The radar echo top (as indicated by 20-dBZ reflectivity contour) reached the 12-km altitude over the southern and eastern part of Typhoon Fanapi. The strong vorticity stretching (STR term in red contour) is mainly concentrated in the TC inner core at lower levels. The low-level vertical shear in horizontal wind (with maximum magnitude of 30 m s^{-1} or above) produced the horizontal vorticity vectors, which were then tilted into the vertical direction by the convective updrafts and downdrafts. Then the convective updrafts transport the vorticity to middle and upper levels through the VHTs (see the strong updrafts and positive vorticities in Fig. 16b).

Based on the above vorticity budget calculations, we propose the conceptual model of eyewall reorganization of Typhoon Fanapi in two perspective views shown in Fig. 22 (from the southeast and northwest). When Typhoon Fanapi passed through Taiwan Island, its eyewall was broken down by the mechanical disruption from the CMR. The strong subsidence that occurred on the lee (western) side of CMR produced a much drier environment, which is a top-down process. The primary rainband in the TC vortex circulation brought vigorous convection from the ocean (the Taiwan Strait), which supplied abundant moisture at lower levels by precipitation evaporation and moisture transport from the oceanic airmass. As a result, the environment became moister and convectively unstable. Deep convection region increased

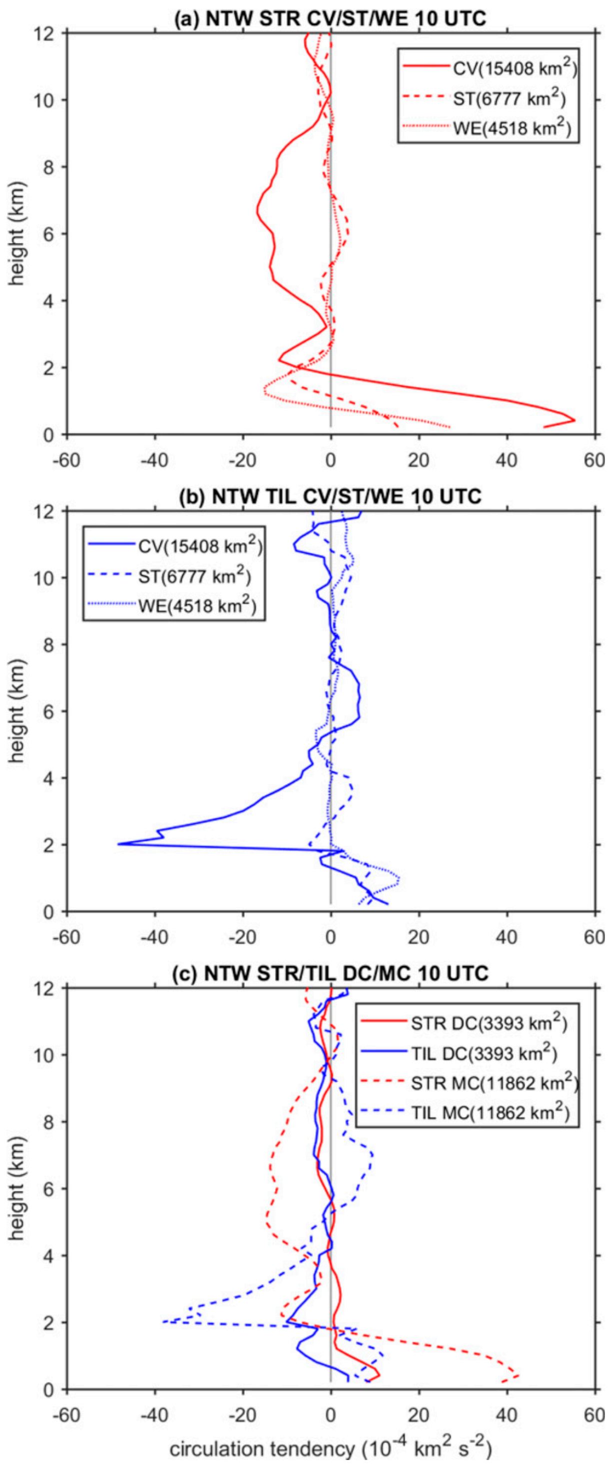

FIG. 21. The vertical profiles of circulation tendency (10^{-4} km^2 s^{-2}) for (a) the STR , (b) TIL terms, and (c) their area-mean values within the deep convection (DC) and moderate convection (MC) regions for NTW experiment at 1000 UTC. (a),(b) The solid line indicates the contribution by the convective region (CV), the dashed line is for the stratiform region (ST), and the dotted line is for the weak and no echo region (WE). The size of each region is indicated in the panel legends.

on the windward (western) side of CMR and produced vertical vorticity through the STR and TIL terms within the boundary layer, which is a bottom-up process. Finally, VHTs transported positive (cyclonic) vorticity from lower to middle levels to complete the eyewall reorganization process, and the eyewall reorganization of Typhoon Fanapi (2010) is indeed a coupling between the bottom-up (major) and top-down (minor) processes.

5. Conclusions

In this study, three WRF simulations—one with the full Taiwan terrain (CTL) and two without the Taiwan terrain (NTR and NTW)—were analyzed. The convective–stratiform separation algorithm developed by Didlake and Houze (2009) was employed on the observed and simulated radar reflectivity data to classify the precipitation regimes. In addition to stratiform and weak-echo regions, the convective region was further divided into deep convection, moderate convection, and shallow convection by different echo-top heights of 20-dBZ radar reflectivity (i.e., greater than 10 km for deep convection, 4–10 km for moderate convection, and lower than 4 km for shallow convection, respectively). The percentage of deep convection increased from 8% to 20% when Typhoon Fanapi had an eyewall reorganization process in the CTL simulation. If the Taiwan terrain were absent, moderate convection would occupy most of the convective region. With the presence of Taiwan terrain, precipitation evaporation and moisture transport from the oceanic airmass on the windward side of the CMR (south to the Fanapi circulation center) provided abundant moisture in the boundary layer. The high equivalent potential temperature air within Fanapi's vortex circulation reached the steep CMR terrain and then produced deep convection, triggering VHTs in the southwestern part of Taiwan.

To analyze the vorticity generation mechanisms in different precipitation regions, a vorticity budget in a TC center-following framework was used in this study. We found that, at the beginning of Fanapi's eyewall reconstruction, the positive vorticity stretching in moderate convection was greater than that in deep convection. Total vorticity stretching in deep convection then increased after the eyewall organization, and later became stronger than that in moderate convection. The Central Mountain Range of Taiwan played the key role in breaking down the eyewall through mechanical disruption, and then rebuilding the eyewall through the enhancement of upslope deep convection as Fanapi passed through the terrain.

Finally, we should keep these caveats in mind that the diagnostics results presented in this study are based on model simulations with typhoon track and intensity errors, model deficiencies, and physics uncertainties. Typhoon Fanapi (2010) is a rare case in the sense that observational data from multiple Doppler ground-based radars are available to analyze the eyewall reorganization and precipitation classification. In the future, more TC cases should be examined in order to generalize the findings from this case to other TCs in mountainous

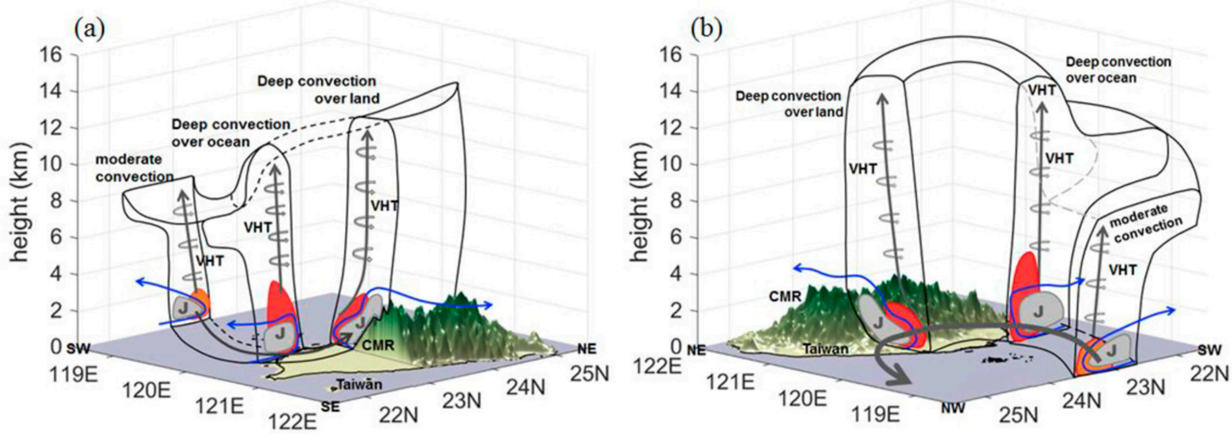

FIG. 22. The conceptual model of eyewall reorganization of Typhoon Fanapi in two perspective views: (a) from the southeast and (b) from the northwest. The black contour indicates the radar-echo isosurface of 20 dBZ, the thick gray arrow and "J" indicate the local maximum tangential wind of Typhoon Fanapi, the red and orange contours indicate the stretching in deep and moderate convection, the blue arrow indicates the tilting of the horizontal vorticity into the vertical direction, and the thin gray curved arrows indicate the vortical hot towers (VHTs).

regions in the Atlantic Ocean and Indian Ocean or near Australia.

Acknowledgments. We thank Central Weather Bureau in Taiwan for providing the radar data. YCW and MJY were supported by the Ministry of Science and Technology in Taiwan under Grants MOST 108-2625-M-052-003 and MOST 108-2111-M-002-011-MY2. RFR was supported by NOAA base funds. The observation data are available from the Typhoon Databank of Central Weather Bureau (http://rdc8.cwb.gov.tw). The ECMWF/TOGA data are available from Research Data Archive (https://rda.ucar.edu/datasets/ds111.1/). The model simulations were performed and archived at National Taiwan University (http://rain.as.ntu.edu.tw/Fanapi.htm).

REFERENCES

Atlas, D., K. R. Hardy, R. Wexler, and R. J. Boucher, 1963: On the origin of hurricane spiral bands. *Geofis. Int.*, **3**, 123–132.

Churchill, D. D., and R. A. Houze Jr., 1984: Development and structure of winter monsoon cloud clusters on 10 December 1978. *J. Atmos. Sci.*, **41**, 933–960, https://doi.org/10.1175/1520-0469(1984)041<0933:DASOWM>2.0.CO;2.

Corbosiero, K. L., and J. Molinari, 2002: The effects of vertical wind shear on the distribution of convection in tropical cyclones. *Mon. Wea. Rev.*, **130**, 2110–2123, https://doi.org/10.1175/1520-0493(2002)130<2110:TEOVWS>2.0.CO;2.

——, and ——, 2003: The relationship between storm motion, vertical wind shear, and convective asymmetries in tropical cyclones. *J. Atmos. Sci.*, **60**, 366–376, https://doi.org/10.1175/1520-0469(2003)060<0366:TRBSMV>2.0.CO;2.

Didlake, A. C., and R. A. Houze Jr., 2009: Convective-scale downdrafts in the principal rainband of Hurricane Katrina (2005). *Mon. Wea. Rev.*, **137**, 3269–3293, https://doi.org/10.1175/2009MWR2827.1.

——, and ——, 2013a: Convective-scale variations in the inner-core rainbands of a tropical cyclone. *J. Atmos. Sci.*, **70**, 504–523, https://doi.org/10.1175/JAS-D-12-0134.1.

——, and ——, 2013b: Dynamics of the stratiform sector of a tropical cyclone rainband. *J. Atmos. Sci.*, **70**, 1891–1911, https://doi.org/10.1175/JAS-D-12-0245.1.

Dudhia, J., 1989: Numerical study of convection observed during the Winter Monsoon Experiment using a mesoscale two-dimensional model. *J. Atmos. Sci.*, **46**, 3077–3107, https://doi.org/10.1175/1520-0469(1989)046<3077:NSOCOD>2.0.CO;2.

Fritz, C., Z. Wang, S. W. Nesbitt, and T. J. Dunkerton, 2016: Vertical structure and contribution of different types of precipitation during Atlantic tropical cyclone formation as revealed by TRMM PR. *Geophys. Res. Lett.*, **43**, 894–901, https://doi.org/10.1002/2015GL067122.

Geerts, B., G. M. Heymfield, L. Tian, J. B. Halverson, A. Guillory, and M. I. Mejia, 2000: Hurricane Georges's landfall in the Dominican Republic: Detailed airborne Doppler radar imagery. *Bull. Amer. Meteor. Soc.*, **81**, 999–1018, https://doi.org/10.1175/1520-0477(2000)081<0999:HGLITD>2.3.CO;2.

Grell, G. A., and D. Dévényi, 2002: A generalized approach to parameterizing convection combining ensemble and data assimilation techniques. *Geophys. Res. Lett.*, **29**, 1693, https://doi.org/10.1029/2002GL015311.

Hence, D. A., and R. A. Houze Jr., 2011: Vertical structure of hurricane eyewalls as seen by the TRMM Precipitation Radar. *J. Atmos. Sci.*, **68**, 1637–1652, https://doi.org/10.1175/2011JAS3578.1.

——, and ——, 2012: Vertical structure of tropical cyclone rainbands as seen by the TRMM Precipitation Radar. *J. Atmos. Sci.*, **69**, 2644–2661, https://doi.org/10.1175/JAS-D-11-0323.1.

Holton, J. R., 2004: *An Introduction to Dynamical Meteorology*. 4th ed. Elsevier Academic Press, 535 pp.

Hong, S.-Y., and H.-L. Pan, 1996: Nonlocal boundary layer vertical diffusion in a medium-range forecast model. *Mon. Wea. Rev.*, **124**, 2322–2339, https://doi.org/10.1175/1520-0493(1996)124<2322:NBLVDI>2.0.CO;2.

Houze, R. A., Jr., 1997: Stratiform precipitation in regions of convection: A meteorological paradox? *Bull. Amer. Meteor. Soc.*, **78**, 2179–2196, https://doi.org/10.1175/1520-0477(1997)078<2179:SPIROC>2.0.CO;2.

Huang, Y.-H., C.-C. Wu, and Y. Wang, 2011: The influence of island topography on typhoon track deflection. *Mon. Wea. Rev.*, **139**, 1708–1727, https://doi.org/10.1175/2011MWR3560.1.

Liou, Y.-C., T.-C. C. Wang, and P.-Y. Huang, 2016: The inland eyewall reintensification of Typhoon Fanapi (2010) documented from an observational perspective using multiple-Doppler radar and surface measurements. *Mon. Wea. Rev.*, **144**, 241–261, https://doi.org/10.1175/MWR-D-15-0136.1.

May, P. T., 1996: The organization of convection in the rainbands of Tropical Cyclone Laurence. *Mon. Wea. Rev.*, **124**, 807–815, https://doi.org/10.1175/1520-0493(1996)124<0807:TOOCIT>2.0.CO;2.

Mlawer, E. J., S. J. Taubman, P. D. Brown, M. J. Iocono, and S. A. Clough, 1997: Radiative transfer for inhomogeneous atmospheres: RRTM, a validated correlated-k model for the longwave. *J. Geophys. Res.*, **102**, 16 663–16 682, https://doi.org/10.1029/97JD00237.

Morrison, H., and A. Gettelman, 2008: A new two-moment bulk stratiform cloud microphysics scheme in the Community Atmosphere Model, version 3 (CAM3). Part I: Description and numerical tests. *J. Climate*, **21**, 3642–3659, https://doi.org/10.1175/2008JCLI2105.1.

——, J. A. Curry, and V. I. Khvorostyanov, 2005: A new double-moment microphysics parameterization for application in cloud and climate models. Part I: Description. *J. Atmos. Sci.*, **62**, 1665–1677, https://doi.org/10.1175/JAS3446.1.

Poujol, B., S. P. Sobolowski, P. A. Mooney, and S. Berthou, 2020: A physically based precipitation separation algorithm for convection-permitting models over complex topography. *Quart. J. Roy. Meteor. Soc.*, **146**, 748–761, https://doi.org/10.1002/qj.3706.

Powell, M. D., 1990: Boundary layer structure and dynamics in outer hurricane rainbands. Part I: Mesoscale rainfall and kinematic structure. *Mon. Wea. Rev.*, **118**, 891–917, https://doi.org/10.1175/1520-0493(1990)118<0891:BLSADI>2.0.CO;2.

Rogers, R. F., 2010: Convective-scale structure and evolution during a high-resolution simulation of tropical cyclone rapid intensification. *J. Atmos. Sci.*, **67**, 44–70, https://doi.org/10.1175/2009JAS3122.1.

——, P. D. Reasor, J. A. Zawislak, and L. T. Nguyen, 2020: Precipitation processes and vortex alignment during the intensification of a weak tropical cyclone in moderate vertical shear. *Mon. Wea. Rev.*, **148**, 1899–1929, https://doi.org/10.1175/MWR-D-19-0315.1.

Schubert, W. H., and J. J. Hack, 1982: Inertial stability and tropical cyclone development. *J. Atmos. Sci.*, **39**, 1687–1697, https://doi.org/10.1175/1520-0469(1982)039<1687:ISATCD>2.0.CO;2.

Skamarock, W. C., and Coauthors, 2008: A description of the Advanced Research WRF version 3. NCAR Tech. Note NCAR/TN-475+STR, 113 pp., https://doi.org/10.5065/D68S4MVH.

Steiner, M., R. A. Houze Jr., and S. E. Yuter, 1995: Climatological characterization of three-dimensional storm structure from operational radar and rain gauge data. *J. Appl. Meteor.*, **34**, 1978–2007, https://doi.org/10.1175/1520-0450(1995)034<1978:CCOTDS>2.0.CO;2.

Tao, C., and H. Jiang, 2015: Distributions of shallow to very deep precipitation–convection in rapidly intensifying tropical cyclones. *J. Climate*, **28**, 8791–8824, https://doi.org/10.1175/JCLI-D-14-00448.1.

Tremblay, A., 2005: The stratiform and convective components of surface precipitation. *J. Atmos. Sci.*, **62**, 1513–1528, https://doi.org/10.1175/JAS3411.1.

Wu, C.-C., T.-H. Li, and Y.-H. Huang, 2015: Influence of mesoscale topography on tropical cyclone tracks: Further examination of the channeling effect. *J. Atmos. Sci.*, **72**, 3032–3050, https://doi.org/10.1175/JAS-D-14-0168.1.

Yang, M.-J., Y.-C. Wu, and Y.-C. Liou, 2018: The study of inland eyewall reconstruction of Typhoon Fanapi (2010) using numerical experiments and vorticity budget analyses. *J. Geophys. Res. Atmos.*, **123**, 9604–9623, https://doi.org/10.1029/2018JD028281.

Yeh, T.-C., and R. L. Elsberry, 1993a: Interaction of typhoons with the Taiwan orography. Part I: Upstream track deflections. *Mon. Wea. Rev.*, **121**, 3193–3212, https://doi.org/10.1175/1520-0493(1993)121<3193:IOTWTT>2.0.CO;2.

——, and ——, 1993b: Interaction of typhoons with the Taiwan orography. Part II: Continuous and discontinuous tracks across the island. *Mon. Wea. Rev.*, **121**, 3213–3233, https://doi.org/10.1175/1520-0493(1993)121<3213:IOTWTT>2.0.CO;2.

Yuter, S. E., and R. A. Houze Jr., 1995: Three-dimensional kinematic and microphysical evolution of Florida cumulonimbus. Part II: Frequency distribution of vertical velocity, reflectivity, and differential reflectivity. *Mon. Wea. Rev.*, **123**, 1941–1963, https://doi.org/10.1175/1520-0493(1995)123<1941:TDKAME>2.0.CO;2.